

1
2 **Cumulus Moistening, the Diurnal Cycle, and**
3 **Initiation of the Madden–Julian Oscillation**
4 **during DYNAMO**
5

6
7 James H. Ruppert, Jr.¹ and Richard H. Johnson
8 Department of Atmospheric Science, Colorado State University, Fort
9 Collins, Colorado
10
11
12
13

¹ *Corresponding author address:* James H. Ruppert, Jr., Department of Atmospheric Science, Colorado State University, Fort Collins, CO 80523.
E-mail: ruppert@atmos.colostate.edu

14
15
16
17
18
19
20
21
22
23
24
25
26
27
28
29
30
31
32
33
34
35
36
37
38
39

Abstract

Atmospheric soundings, cloud radar, and air-sea flux measurements collected during DYNAMO (Dynamics of the MJO) are employed to study the initiation of the Madden–Julian Oscillation (MJO) over the tropical Indian Ocean. Findings indicate that moistening of the troposphere during MJO initiation occurs in two stages: low-to-midlevel moistening in the suppressed phase (i.e., prior to the onset of deep convection), followed by deep-column moistening during the early active phase. The first stage of moistening is accomplished by a population of shallow cumulus and congestus clouds, and is orchestrated by the waning of large-scale subsidence and horizontal-advective drying, which enables the persistent cumulus field to ultimately humidify the column and deepen. Following the onset of deep convection, deep-column moistening occurs in conjunction with a bottom-heavy diabatic heating profile, indicative of predominant congestus and cumulonimbus clouds. *Analysis of the suppressed phase reveals the striking degree to which the moistening characteristic of this period is accomplished by the diurnal cycle of cumulus clouds.* This diurnal cycle is driven by the cycle in sea surface temperature and air-sea fluxes linked to shallow oceanic diurnal warm layers. This coupled diurnal cycle, and the associated afternoon peak in convective cloud depth, cloud areal coverage, and cumulus moistening, likely drives more vigorous overall moistening than would occur without this diurnal cycle. *A conspicuous finding pertaining to the suppressed phase convection is the prominence of mesoscale cloud organization (i.e., open cells and horizontal convective rolls),* which is hypothesized to enhance convective instability in localized patches, thereby promoting deeper, more vigorous cumulus moistening than would otherwise occur.

40

41

1. Introduction

42 The Madden–Julian Oscillation (MJO; Madden and Julian 1971, 1972) dominates
43 tropical intraseasonal (20–90-day) variability and influences global weather through
44 myriad tropical–extratropical teleconnections (Zhang 2005, 2013). Through these
45 teleconnections the MJO acts as a “bridge” between weather and climate (Zhang 2013),
46 thereby holding a critical key to our advancement beyond medium-range predictability
47 (Hendon et al. 2000; Waliser et al. 2003, 2012; Lin et al. 2006; Moncrieff et al. 2012).
48 While advances have been made in the understanding of propagation, diabatic heating
49 structure, and convective cloud properties of the MJO, the processes that govern MJO
50 initiation—the primary transition from shallow to deep moist convection—remain in
51 question (Bladé and Hartmann 1993; Johnson et al. 1999; Stephens et al. 2004; Zhang
52 2005; Majda and Stechmann 2009; Waite and Khouider 2010; Jiang et al. 2011; Sobel et
53 al. 2014). The foremost hindrance in this regard is a lack of key in situ observations in
54 the tropical Indian Ocean where MJO initiation takes place (Madden and Julian 1972;
55 Hendon and Salby 1994; Wheeler and Hendon 2004).

56 Investigating MJO initiation was a central objective of the DYNAMO (Dynamics
57 of the MJO) field campaign, which was conducted in the tropical Indian Ocean during
58 2011–12 boreal fall–winter in collaboration with CINDY (Cooperative Indian Ocean
59 Experiment on Intraseasonal Variability in the Year 2011), AMIE (ARM MJO
60 Investigation Experiment), and LASP (Littoral Air-Sea Processes) (Yoneyama et al.
61 2013; Zhang et al. 2013). Hereafter, these efforts will be referred to collectively as

62 DYNAMO. Two MJO events were comprehensively sampled in DYNAMO, providing
63 an unprecedented opportunity to diagnose the key processes in MJO initiation.

64 The MJO is a planetary-scale (zonal wavenumber 1–2) overturning circulation
65 that propagates eastward across the tropical eastern hemisphere at $\sim 5 \text{ m s}^{-1}$, with heavy
66 rainfall in its *active phase* and little-to-no rainfall in its *suppressed phase* (Madden and
67 Julian 1972; Zhang 2005). During the transition from suppressed to active conditions,
68 from an Eulerian viewpoint, the prevailing character of convective clouds evolves from
69 shallow cumulus, to congestus, to deep cumulonimbus and stratiform as the free
70 troposphere transitions from dry, to moist up to midlevels, to fully moistened,
71 respectively (Johnson and Lin 1997; DeMott and Rutledge 1998; Johnson et al. 1999;
72 Kikuchi and Takayabu 2004; Benedict and Randall 2007; Haertel et al. 2008; Yoneyama
73 et al. 2008; Waite and Khouider 2010; Riley et al. 2011; Del Genio et al. 2012). This
74 well-documented coupling between moist convection and column humidity within the
75 MJO, which is self-similar in space and time (Mapes et al. 2006), fundamentally owes to
76 the buoyancy-limitation that dry air in the lower-free troposphere imposes on ascending
77 moist-convective plumes (Austin 1948; Wei et al. 1998; Redelsperger et al. 2002; Takemi
78 et al. 2004; Holloway and Neelin 2009). In light of this coupling, the paradigm
79 describing the MJO as a *moisture mode* has gained much ground in recent years
80 (Raymond 2001; Sobel et al. 2001).

81 Within the framework of moisture-mode theory, intraseasonal anomalies in moist
82 convection and column humidity evolve in unison under the constraints of weak
83 temperature gradient (WTG) theory; and therefore, processes that augment column
84 humidity (or moist static energy, MSE) also augment the convection (Raymond 2001;

85 Sobel et al. 2001; Raymond and Fuchs 2009; Raymond et al. 2009; Hannah and Maloney
86 2011). Under this framework, diagnosis of the vertically integrated MSE budget has
87 elucidated important aspects of MJO dynamics—namely, propagation and maintenance.
88 MJO propagation is fundamentally driven by the Gill response to large-scale diabatic
89 heating (Gill 1980), i.e., the enhancement (suppression) of equatorward advection of dry
90 air from higher latitudes by equatorial Rossby waves on the west (east) side of the MJO
91 active phase (Chen et al. 1996; Maloney and Hartmann 1998; Benedict and Randall 2007;
92 Maloney 2009; Maloney et al. 2010; Sobel and Maloney 2013; Kerns and Chen 2014;
93 Sobel et al. 2014). A growing body of evidence suggests that the MJO, as a moisture
94 mode, is maintained and/or amplified by a feedback between the large-scale envelope of
95 deep convection and column radiative heating (Hu and Randall 1994; Yu et al. 1998;
96 Raymond 2001; Chikira 2014; Sobel et al. 2014).

97 Despite the above advances, the question of what governs MJO initiation—the
98 development of large-scale diabatic heating—remains open. Understanding MJO
99 initiation and the associated onset of large-scale diabatic heating is crucial, since this
100 onset gives rise to the large-scale circulation pattern and radiative feedbacks key to MJO
101 propagation and maintenance. Furthermore, proper representation of MJO initiation—a
102 difficulty for many models at present—is critical to accurate prediction of the many
103 global weather patterns that are remotely linked to the MJO diabatic heat source
104 (Moncrieff et al. 2012; Zhang 2013).

105 *Owing to DYNAMO, the relationships between moist convection and the large-*
106 *scale environment during MJO initiation can now be diagnosed from in situ*
107 *observations.* This study carries out such a diagnosis in two steps, as follows. In section

108 3, sounding data are employed to compare the apparent heating Q_1 and drying Q_2 , the
109 column-integrated moisture budget, and radar-deduced convective cloud information for
110 the two DYNAMO MJO events. This large-scale analysis seeks to identify the key
111 processes at play in MJO initiation, thereby laying the groundwork for section 4. Section
112 4 provides a more detailed analysis of the governing processes in the primary period of
113 moistening prior to MJO onset (i.e., the onset of deep convection). Many studies argue
114 that this period of moistening in the suppressed phase, often called the *preconditioning* or
115 *recharge* phase, is crucial to MJO initiation (Hendon and Liebmann 1990; Rui and
116 Hartmann 1990; Bladé and Hartmann 1993; Maloney and Hartmann 1998; Johnson et al.
117 1999; Benedict and Randall 2007). A key finding of this study is that the low-to-
118 midlevel moistening (or preconditioning) during the suppressed phase is accomplished by
119 a population of shallow cumulus and congestus clouds that exhibits a pronounced diurnal
120 cycle in response to oceanic diurnal warm layers, as well as marked mesoscale
121 organization (i.e., open cells and horizontal convective rolls). The implications of these
122 findings are discussed along with summary and conclusions in section 5.

123

124 2. Data and Methods

125 The primary DYNAMO observations employed in this study, which include those
126 from a sounding network, a cloud-sensitive radar, and an air-sea flux site, are available
127 from http://data.eol.ucar.edu/master_list/?project=DYNAMO.

128

129 *Gridded sounding analysis*

130 The Indian Ocean sounding network was composed of six sites, making two
131 quadrilaterals straddling the equator, 500~800 km on a side. The signals of the two (Oct
132 and Nov) MJO events were well sampled by the northern quadrilateral, while the
133 southern quadrilateral sampled intermittent deep convection connected to the ITCZ
134 (intertropical convergence zone; Johnson and Ciesielski 2013). The analysis is therefore
135 limited to the northern quadrilateral (Fig. 1). This quadrilateral was comprised by three
136 islands—Gan, Malé, and Colombo—and a ship site—the R/V *Revelle*. Katsumata et al.
137 (2011) demonstrate that a four-point quadrilateral array accurately samples both the
138 divergent and rotational flow components comprising the large-scale MJO circulation,
139 while a triangular array does a poorer job. Therefore, periods when the R/V *Revelle* went
140 offsite and the sounding array was reduced to three points are indicated in the figures.

141 A comprehensive set of quality-control techniques has been applied to the
142 DYNAMO soundings, including mitigation of the low-level heat island and flow
143 blocking effects in the Colombo soundings due to the large island of Sri Lanka
144 (Ciesielski et al. 2014a,b). Following quality control, the sounding observations were
145 horizontally interpolated onto a 0.25° mesh using the multiquadric objective analysis
146 technique of Nuss and Titley (1994), and vertically interpolated onto an isobaric grid at
147 25-hPa spacing from 1000–50 hPa. Several observational datasets (dropsondes, satellite-
148 derived vector winds, scatterometer surface winds, and thermodynamic profiles from
149 radio occultation measurements) were included in the interpolation to supplement the
150 soundings, the details of which can be found in a companion paper (Johnson et al. 2014,

151 submitted to *J. Atmos. Sci.*). The gridded analysis was then spatially averaged over the
152 northern sounding array to yield a time–pressure series of mean northern-array quantities.

153 During the special observing period (SOP: 1 Oct–15 Dec), soundings were
154 launched eight (four) times per day at the equatorial (northern) sites (Fig. 1), though on 8
155 Dec launches at Colombo reduced to one per day. Therefore, the analysis will be carried
156 out for 1 Oct–7 Dec. Temporal interpolation was carried out to generate data at three-
157 hourly frequency at the two northern sites (Fig. 1). This procedure was crucial for
158 exploiting the three-hourly information from the two equatorial sites, which resulted in
159 markedly improved sampling of the diurnal cycle. The interpolation was performed for
160 the analysis times of 0300, 0900, 1500, and 2100 UTC using the two soundings from
161 three hours prior to and following the analysis time for the respective site (interpolation
162 was not performed if either of these surrounding soundings were missing). The error due
163 to this procedure was assessed by exploiting the three-hourly soundings at Gan. RMS
164 differences between actual and contemporaneous soundings generated by this procedure
165 amounted to $\sim 0.5^{\circ}\text{C}$, 0.5 g kg^{-1} , and 1 m s^{-1} in temperature, specific humidity, and wind
166 speed, respectively, which are inconsequential for the objectives of this study.

167 Similar analysis approaches to those described above have been successfully
168 applied in many previous tropical and monsoon field campaigns (e.g., the Tropical Ocean
169 Global Atmosphere Coupled Ocean–Atmosphere Response Experiment, or COARE, the
170 South China Sea Monsoon Experiment, the North American Monsoon Experiment, and
171 the Terrain-influenced Monsoon Rainfall Experiment), which have confirmed the
172 reliability of results via comparison with independent observations (Lin and Johnson
173 1996a,b; Johnson and Ciesielski 2002; Ciesielski et al. 2003; Johnson et al. 2010;

174 Ruppert et al. 2013). Detailed comparisons between the DYNAMO gridded sounding
175 analysis and independent datasets are provided by Johnson et al. (2014), and are not
176 repeated here. Provided in section 3, however, is a comparison between budget-derived
177 and satellite-measured rainfall, demonstrating marked consistency between the two
178 datasets.

179

180 *Radar cloud measurements*

181 The behavior of clouds is assessed using measurements from the National Center
182 for Atmospheric Research (NCAR) dual-polarimetric and dual-frequency (10 cm: S band,
183 and 8 mm: Ka band) S-Pol weather research radar (Keeler et al. 2000), which was
184 deployed on Addu Atoll (just south of Gan Island; 0.63°S, 73.10°E), Maldives, during
185 DYNAMO (only S-band data are employed in this study). The details of S-Pol data
186 quality control and field instrumentation management can be found at
187 <https://www.eol.ucar.edu/instrumentation/remote-sensing/s-pol> and in prior studies that
188 have employed this dataset (Powell and Houze 2013; Zuluaga and Houze 2013; Rowe
189 and Houze 2014). When viewing S-Pol data in this study, the caveat that the S-Pol
190 sampling region is far smaller than and on the corner of the northern sounding array must
191 be considered. Slight inconsistencies in timing between northern array-averaged
192 quantities and radar quantities are possible due to this issue.

193 Owing to its high sensitivity, the S-Pol detects non-precipitating clouds, which are
194 important in moistening the lower troposphere (Nitta and Esbensen 1974; Johnson and
195 Lin 1997). This study employs the range–height indicator (RHI) measurements from the
196 S-Pol northeastern quadrant dataset, which is composed of vertical slices over azimuths

197 from 4°–82° (where there is minimal ground clutter) at 2° intervals, up to an elevation
198 angle of 40°, and at 15-min sampling frequency. The maximum range of the RHI
199 measurements is 150 km, though data are only retained within a 50-km range for this
200 analysis, within which the loss of radar sensitivity is minor (Feng et al. 2014). A subset
201 of echo-base and echo-top height measurements is assembled from the dataset following
202 interpolation of the data onto a Cartesian grid of 500-m vertical–horizontal spacing.
203 Echo base and top are defined as the vertical boundaries of contiguous detectable echo
204 return, with a minimum echo threshold of –30 dBZ (Feng et al. 2014). The echo features
205 selected for this analysis include those with a base elevation ≤ 1 km and vertical depth \geq
206 1.5 km, thereby effectively excluding very thin clouds and Bragg scattering layers related
207 to detrained moisture and turbulent mixing across vertical moisture gradients (Davison et
208 al. 2013). What are left are boundary layer-based clouds and raining high-based clouds.
209 During suppressed periods, when rainfall is minimal and stratiform systems rare, these
210 echo features are dominated by boundary layer-based convective clouds (Powell and
211 Houze 2013; Zuluaga and Houze 2013; Rowe and Houze 2014). Furthermore, since the
212 tropical environment is always conditionally unstable, features terminating below the
213 mid-tropospheric level of minimum in MSE are almost certainly convective.

214 *Echo-top frequency* is calculated from the above-described subset of echo features
215 by counting the total occurrences of echo top at each vertical level as a function of time,
216 and normalizing this result by the total number of grid bins in the horizontal plane. *Echo*
217 *area coverage* is calculated from the same subset by dividing the total number of
218 horizontal grid points containing echo (at any level, subject to the above criteria) by the
219 total number of grid points in the horizontal plane.

220

221 *Auxiliary datasets*

222 High-time-resolution (10-min) thermodynamic variables were collected during
223 DYNAMO at the R/V *Revelle*. The measurements employed herein include sea surface
224 temperature (SST), which has been adjusted to skin temperature, surface sensible and
225 latent heat flux, wind speed, wind stress, and 10-m air temperature and humidity. Daily-
226 mean latent heat flux from the TropFlux product (Praveen Kumar et al. 2011) is
227 employed following an average over the northern sounding quadrilateral to facilitate the
228 estimation of rainfall from the moisture budget. The TRMM (Tropical Rainfall
229 Measurement Mission; Kummerow et al. 2000) 3B42v7 rainfall product (three-hourly
230 frequency; Huffman et al. 2007) is employed, following an average over the northern
231 sounding quadrilateral, for comparison with budget-derived rainfall. Orbit swath true-
232 color images from MODIS (Moderate Resolution Imaging Spectroradiometer) are also
233 employed, which are collected from [http://lance-modis.eosdis.nasa.gov/cgi-](http://lance-modis.eosdis.nasa.gov/cgi-bin/imagery/realtime.cgi)
234 [bin/imagery/realtime.cgi](http://lance-modis.eosdis.nasa.gov/cgi-bin/imagery/realtime.cgi).

235

236 3. Convection and the large-scale environment during MJO 237 initiation

238 Two complete MJO cycles were sampled by the DYNAMO northern sounding
239 array during its full operation—one in Oct (MJO1) and one in Nov (MJO2). These MJO
240 events are reflected in Fig. 2 as periods of very dry conditions (i.e., relative humidity RH
241 < 50%) through a deep layer with little-to-no rainfall—the *suppressed phase* (MJO1:

242 early–mid Oct; MJO2: mid Nov)—followed by very moist conditions (i.e., RH > 70%)
243 with enhanced rainfall—the *active phase* (MJO1: late Oct–early Nov; MJO2: late Nov).
244 (MJO sub-periods indicated in Fig. 2 and subsequent figures are defined later.)
245 Differences in MJO event duration are apparent, with both the suppressed and active
246 phases of MJO1 outlasting those of MJO2 by roughly one week.

247 The bottom-up moistening that commences as light rainfall begins during the
248 suppressed phase has been noted in numerous studies, and is often referred to as the
249 *preconditioning* or *recharging* stage of the MJO (Fig. 2) (Bladé and Hartmann 1993; Lin
250 and Johnson 1996a,b; Johnson et al. 1999; Kikuchi and Takayabu 2004; Kiladis et al.
251 2005; Benedict and Randall 2007; Haertel et al. 2008). The character of this low-to-
252 midlevel moistening differs between MJO1 and MJO2, as described later. Moistening
253 from aloft can also be noted in Fig. 2 (e.g., from 15~20 Nov in the layer 150–300 hPa),
254 which owes to the adiabatic cooling forced by an eastward-propagating Kelvin wave due
255 related to an earlier MJO event (Kiladis et al. 2001; Gottschalck et al. 2013; Johnson and
256 Ciesielski 2013). Prior studies have noted an increase in the frequency of cirrus clouds in
257 the upper troposphere–lower stratosphere in the days–weeks prior to the MJO active
258 phase, which may relate to such Kelvin waves (Virts and Wallace 2010; Virts et al. 2010;
259 Riley et al. 2011; Del Genio et al. 2012). Powell and Houze (2014, submitted to *J.*
260 *Geophys. Res.*) argue that the upper-tropospheric divergence associated with this feature
261 links to an increase in stratiform precipitation systems around the time of MJO initiation.
262 It is yet unclear, however, whether or not this divergence is linked to the observed
263 moistening in the low–midtroposphere.

264 Figure 3 provides DYNAMO daily-averaged time–pressure series of the apparent
 265 heat source Q_1 and apparent moisture sink Q_2 , calculated as follows (Yanai et al. 1973):

$$266 \quad Q_1 \equiv \frac{D\bar{s}}{Dt} = \frac{\partial\bar{s}}{\partial t} + \bar{\mathbf{v}} \cdot \nabla\bar{s} + \bar{\omega} \frac{\partial\bar{s}}{\partial p} = Q_R + L_v(\bar{c} - \bar{e}) - \frac{\partial}{\partial p}(\overline{\omega's'}), \quad (1)$$

$$267 \quad Q_2 \equiv -L_v \frac{D\bar{q}}{Dt} = -L_v \left(\frac{\partial\bar{q}}{\partial t} + \bar{\mathbf{v}} \cdot \nabla\bar{q} + \bar{\omega} \frac{\partial\bar{q}}{\partial p} \right) = L_v(\bar{c} - \bar{e}) + L_v \frac{\partial}{\partial p}(\overline{\omega'q'}), \quad (2)$$

268 with $s = c_p T + gz$ dry static energy, c_p the specific heat of dry air at constant pressure, T
 269 temperature, g gravity, z height, \mathbf{v} horizontal flow, ω vertical pressure velocity, Q_R
 270 radiative heating, L_v the latent heat of vaporization at 0°C, c (e) hydrometeor
 271 condensation (evaporation) rate, and q water vapor mixing ratio. Overbars denote a
 272 spatial average over the northern sounding array, and primes deviations from that
 273 average. The heat and moisture source terms related to horizontal eddies and ice-phase
 274 processes do not appear in (1) and (2), although they can be included (Arakawa and
 275 Schubert 1974; Yanai and Johnson 1993). MJO1 and MJO2 appear clearly in Fig. 3 and
 276 the time series of ω in Fig. 4. Specifically, Q_1 and Q_2 are negative through most of the
 277 troposphere during the suppressed phases in connection with radiative cooling and
 278 moistening by clouds under subsidence; and Q_1 and Q_2 are positive during the two active
 279 phases, reflecting the large latent heating and drying due to precipitation under strong
 280 ascent. *MJO onset* henceforth refers to the time at which subsidence and apparent
 281 cooling and moistening switch to ascent and heating and drying (MJO1: 14 Oct; MJO2:
 282 17 Nov), which is indicated in all relevant figures. As Yanai et al. (1973) show, the
 283 vertically integrated budgets can be written as

$$284 \quad \langle Q_1 \rangle = \langle Q_R \rangle + \langle L_v(\bar{c} - \bar{e}) \rangle - \left\langle \frac{\partial}{\partial p}(\overline{\omega's'}) \right\rangle = \langle Q_R \rangle + L_v P_0 + S_0, \quad (3)$$

$$285 \quad \langle Q_2 \rangle = \langle L_v (\bar{c} - \bar{e}) \rangle + \left\langle L_v \frac{\partial}{\partial p} (\overline{\omega'q'}) \right\rangle = L_v (P_0 - E_0), \quad (4)$$

286 where

$$287 \quad \langle \rangle = \frac{1}{g} \int_{p_T}^{p_{sfc}} () dp,$$

288 P_0 is precipitation, S_0 is surface sensible heat flux, E_0 is surface evaporation rate, p_{sfc} is
 289 surface pressure, and p_T is 50 hPa. P_0 (time series shown in Fig. 2) is calculated from (4)
 290 using E_0 from TropFlux averaged over the northern sounding array. Correlation r
 291 between TRMM rainfall and P_0 is 0.94 (significant to the 99% level; see caption). There
 292 are times when P_0 is slightly negative or departs measurably from TRMM rainfall, which
 293 could owe to any of several factors, including observational sampling errors (Mapes et al.
 294 2003), inaccuracies in E_0 from TropFlux, changes in cloud volume (which break the
 295 assumption that $P_0 = \langle \bar{c} - \bar{e} \rangle$; McNab and Betts 1978), or inaccuracies in TRMM rainfall
 296 (Liu et al. 2007). The marked agreement between P_0 and TRMM rainfall, however, lends
 297 confidence to the gridded sounding analysis, and the moisture budget presented next.

298 Sobel et al. (2014, submitted to *J. Atmos. Sci.*) describe the vertically integrated
 299 MSE budget from DYNAMO observations, which indicates the role of horizontal
 300 advection and convection–radiative heating feedbacks in MJO propagation and
 301 maintenance, respectively, during DYNAMO. The effects of latent heating and vertical
 302 eddy transport by clouds, however, are largely removed from the column-integrated MSE
 303 budget (e.g., Chikira 2014). In this regard, the column-integrated water vapor budget is
 304 better suited for the objectives of this study. From (2) and (4), the column-integrated
 305 water vapor budget can be written as

$$\begin{aligned}
306 \quad \left\langle \frac{\partial L_v \bar{q}}{\partial t} \right\rangle &= -\langle \bar{\mathbf{v}} \cdot \nabla L_v \bar{q} \rangle - \left\langle \bar{\omega} \frac{\partial L_v \bar{q}}{\partial p} \right\rangle - \langle Q_2 \rangle \\
307 \quad &= -\langle \bar{\mathbf{v}} \cdot \nabla L_v \bar{q} \rangle - \left\langle \bar{\omega} \frac{\partial L_v \bar{q}}{\partial p} \right\rangle + L_v (E_0 - P_0). \quad (5)
\end{aligned}$$

308 According to (5), local moistening or drying is driven by horizontal and vertical
309 advection—the resolved processes—as well as surface evaporation and precipitation—
310 the unresolved processes, or the *apparent* sources and sinks, respectively. Since the
311 ambient air outside of clouds in the tropics is always subsiding (i.e., drying), moistening
312 via vertical advection (i.e., ascending motion) in (5) relates to the transport of moisture
313 by in-cloud motions, which dominate the sampled divergent circulation in such scenarios
314 (e.g., Arakawa and Schubert 1974; Yanai et al. 1973; Chikira 2014). While the budget
315 terms, shown in Fig. 5, are smoothed, no means are removed; therefore, their individual
316 contributions to column moistening are conveyed in the absolute sense.

317 Before discussing the individual terms in the moisture budget, three subdivisions
318 of the two MJO events are defined based on several key characteristics and transition
319 points, as depicted in Figs. 2–4. These subdivisions, depicted by shaded bars in all
320 relevant figures, are defined through assessment of daily-mean, unsmoothed fields (not
321 shown). The suppressed phases (“SP”) are identified as the periods in which $\langle Q_2 \rangle < 0$
322 and subsidence prevails prior to MJO onset (1–13 Oct and 10–16 Nov; end-dates are
323 inclusive). These periods are analogous to the *pre-onset stage*, as it is called in
324 DYNAMO parlance (Yoneyama et al. 2013). The active phases are split into two sub-
325 periods each. The first sub-periods are those with distinctly bottom-heavy Q_1 , Q_2 , and ω
326 profiles (“BH”; 14–19 Oct and 17–21 Nov), which correspond with positive local q -
327 tendency (Fig. 5). The second are those characterized by top-heavy Q_1 , Q_2 , and ω

328 profiles (“TH”), which exhibit progressively decreasing local q -tendency (20 Oct–4 Nov
329 and 22–30 Nov).

330 The signs of Q_1 and Q_2 during SP (Fig. 3) indicate, respectively, that from (3) the
331 magnitude of $\langle Q_R \rangle$ exceeds that of S_0 (assuming $S_0 > 0$), and from (4) that the Q_2 signal
332 owes primarily to $E_0 > 0$ (4), since $P_0 \sim 0$ (Fig. 2). Figure 5 reveals that this Q_2
333 moistening due to evaporation works against the drying by subsidence and horizontal
334 advection (mostly zonal advection; not shown). The quasi-balance between large-scale
335 drying and cumulus moistening is analogous to the tropical trade cumulus-like regimes
336 documented previously, though horizontal advection does not play a large role in such
337 regimes (Nitta and Esbensen 1974; Johnson and Lin 1997).

338 In SP/MJO1, the local q -tendency becomes positive around 7 Oct. The low-to-
339 mid-tropospheric moistening observed during the subsequent ~six days is accomplished
340 by surface evaporation (4) and vertical eddy cloud transport (2), which overcomes the
341 drying by large-scale circulation (Figs. 2, 4, and 5). The waning of subsidence and
342 horizontal-advective drying, while cumulus moistening persists, orchestrates the
343 evolution of the local moisture tendency. This reduction in subsidence may be aided by
344 the arrival of Kelvin wave-induced upper-level divergence (Virts and Wallace 2010;
345 Gottschalek et al. 2013; Powell and Houze 2014).

346 In contrast to SP/MJO1, a period of low-to-mid-tropospheric moistening takes
347 place early in SP/MJO2 (Figs. 2 and 5), followed by a persistent period of relatively
348 moist conditions compared to SP/MJO1 (i.e., $\text{RH} \geq 50\%$ up to ~550 hPa). There is little
349 subsequent humidification prior until MJO onset, the beginning of BH/MJO2. Many past
350 MJO studies depict the moist layer building from a shallow depth over the course of a

351 more continuous several-day period, as occurs in SP/MJO1 (Lin and Johnson 1996a;
352 Kiladis et al. 2005; Benedict and Randall 2007; Yoneyama et al. 2008; Riley et al. 2011;
353 Del Genio et al. 2012). Therefore, the moister conditions in SP/MJO2, as well as the
354 nature of this humidification, may be unique.

355 At the time of onset in both MJOs, Q_2 switches to drying due to rainfall as vertical
356 advection switches to a moisture source. The sign-reversal of vertical advection reflects
357 that the rising motion in clouds now dominates the large-scale divergent circulation.
358 Horizontal advection is weakly moistening in the early active phase MJO1. Local
359 moistening persists during BH, which reflects the full-column humidification as the
360 large-scale envelope of deep convection intensifies (Figs. 2–5). This second stage of
361 moistening is accomplished in the presence of bottom-heavy convection (Figs. 3 and 4),
362 indicative of predominant congestus and cumulonimbus clouds. The bottom-heavy
363 heating implies that convective inflow (i.e., convergence) is focused over a shallow depth
364 of the lower-troposphere, leading to a large moisture source that exceeds the sink due to
365 precipitation (Fig. 5) (Wu 2003; Zhang et al. 2004; Chikira 2014).

366 During TH, a switch to local drying occurs, aided by increased horizontal-
367 advective drying. This drying relates to dry intrusions (e.g., Mapes and Zuidema 1996)
368 associated with equatorward advection of dry air in Rossby gyres on the west side of the
369 active phase (Gill 1980; Kerns and Chen 2014). Unsaturated downdrafts in stratiform
370 precipitation systems also assist the drying, as corroborated by progressively more top-
371 heavy convection (Figs. 3 and 4) (Zipser 1977; Powell and Houze 2013; Rowe and
372 Houze 2014). The end of each active phase is met with a return to conditions
373 characteristic of SP.

374 A DYNAMO time series of echo-top frequency and echo area coverage is
375 provided in Fig. 6. An abundance of short-timescale modes is clear in echo-top
376 frequency, particularly the two-day variability during the active phase of MJO1, due to
377 the two-day waves described in past studies (Haertel et al. 2008; Zuluaga and Houze
378 2013). There is also a clear, slower evolution related to the MJO. Shallow and congestus
379 clouds with tops mostly < 10 km prevail during SP (clouds are generally deeper in
380 SP/MJO2, consistent with a deeper moist layer; Fig. 2), with a progressive deepening of
381 clouds prior to and around MJO onset, and tops > 12 km prevailing thereafter during the
382 active phase. Echo area coverage increases from ~ 10 to $\sim 30\%$ during this transition,
383 indicating that cloud systems are both deepening and increasing in abundance and/or size
384 leading up to and shortly after MJO onset. The periods of increasing echo area coverage
385 closely correspond to the periods of column moistening, during which time large-scale
386 diabatic heating is amplifying (Figs. 2–6). This correspondence, under moisture-mode
387 theory, implies reduced or negative *gross moist stability*, i.e., self-amplification of the
388 moisture–convection anomaly (Raymond et al. 2009; Sobel et al. 2014).

389 The findings of this section indicate that humidification of the lower troposphere
390 occurs in two stages. The first stage occurs prior to MJO onset, i.e., during the
391 suppressed phase or pre-onset stage, and is accomplished by surface evaporation (4) and
392 vertical eddy transport (2) connected to a growing (in both depth and areal coverage)
393 population of shallow cumulus and congestus clouds (Figs. 2–6). This humidification
394 and the associated convective invigoration occur as the drying by large-scale circulation
395 wanes, which evidently orchestrates this evolution. The second stage of moistening
396 occurs after MJO onset in connection with bottom-heavy diabatic heating, which

397 correspondingly amplifies as the column continues to moisten (Figs. 2–6). The switch to
398 local drying occurs following a shift to more top-heavy diabatic heating, and is assisted
399 by increasing horizontal dry-air advection. This evolution is consistent with the findings
400 of previous studies (Maloney and Hartmann 1998; Johnson et al. 1999; Kikuchi and
401 Takayabu 2004; Mapes et al. 2006; Benedict and Randall 2007; Del Genio et al. 2012).

402 The processes responsible for the initial moistening of the lower troposphere
403 during the suppressed phase (Fig. 2), i.e., the preconditioning leading to the subsequent
404 onset of deep convection (Bladé and Hartmann 1993; Benedict and Randall 2007),
405 remain unclear. The next section exploits the unique opportunity afforded by DYNAMO
406 to explore these processes. It will be shown that the moistening characteristic of these
407 periods (Figs. 3 and 5) is driven by a diurnally oscillating shallow–congestus cloud
408 population that exhibits marked mesoscale organization. The ocean plays an important
409 role in driving this diurnal cycle.

410

411 4. The role of the diurnal cycle in cumulus moistening

412 Time–pressure series of Q_2 spanning the two MJO suppressed phases reveal
413 substantial short-timescale variability in the shallow cumulus-driven moistening of these
414 periods (Fig. 7). Most prominent of this variability is the diurnal cycle, with moistening
415 often peaking in the afternoon. Late in the Oct suppressed phase (i.e., 9~14 Oct), a subtle
416 increase in the depth of diurnal moistening is evident, which coincides with convective
417 cloud deepening (Fig. 6). Despite the apparent day-to-day variability, the relationships
418 between independent datasets portray a coherent diurnal cycle in moist convection
419 (shown later). This diurnal cycle differs from that of more disturbed regimes, wherein

420 deep convection amplifies overnight due to nocturnally enhanced radiative cooling (Gray
421 and Jacobson 1977; Randall et al. 1991; Xu and Randall 1995; Chen and Houze 1997;
422 Sui et al. 1998; Dai 2001; Yang and Smith 2006; Johnson 2011). The diurnal cycle in
423 suppressed conditions, rather, is driven by the diurnal cycle in the upper ocean.

424 A time series of SST from the R/V *Revelle* during DYNAMO depicts a very
425 prominent diurnal cycle, among other modes of variability (Fig. 8). The diurnal cycle is
426 most regular and/or largest during the suppressed periods when SST_{daily} (SST smoothed
427 with a 24-h running mean) is climbing, with the greatest diurnal increase appearing on 16
428 Nov, from 29.3–32.05°C over the period 0650–1530 LT, i.e., an increase of 2.75°C in 9
429 h! Similar rapid warming was observed during the light-wind periods in COARE (Weller
430 and Anderson 1996). These large diurnal SST swings occur under clear, light-wind
431 conditions owing to the formation of upper-ocean diurnal warm layers, whereby daytime
432 heating stabilizes the upper ocean, inhibits vertical mixing, and hence concentrates
433 subsequent solar heating to within this surface layer (Halpern and Reed 1976; Stramma et
434 al. 1986; Flament et al. 1994; Webster et al. 1996; Weller and Anderson 1996; Kawai and
435 Wada 2007; Bellenger et al. 2010). Greater wind speeds limit the diurnal SST range by
436 enhancing vertical mixing, as in SP/MJO1 (Fig. 8). In spite of more limited diurnal SST
437 range, however, the response in clouds can still be large (Fig. 7).

438 Time series of surface flux measurements from the R/V *Revelle* spanning
439 SP/MJO1 (Fig. 9) and SP/MJO2 (Fig. 10) corroborate the prominence of the diurnal
440 cycle during these periods. During SP/MJO1, sensible heat flux (S_0) and 10-m air
441 temperature often exhibit diurnal cycles closely following that of SST, though wind
442 speed and latent heat flux ($L_v E_0$) are dominated by longer-timescale variability. During

443 SP/MJO2, however, SST, air temperature, S_0 , $L_v E_0$, and wind speed all exhibit clear
444 diurnal cycles, particularly in the four days leading up to MJO onset. The relationship
445 between variables is more clearly depicted in Fig. 11, which shows anomaly diurnal
446 composites over the strongly diurnally modulated days. These composites are calculated
447 by averaging the time series as a function of time of day and removing the composite
448 mean. During the period in SP/MJO2, there is a composite-average night–day SST
449 variation of $\sim 1.5^\circ\text{C}$, with a peak at ~ 13 local time (13L). Night–day variations in air
450 temperature, S_0 , $L_v E_0$, and wind speed are $\sim 1^\circ\text{C}$, $\sim 10 \text{ W m}^{-2}$, $\sim 80 \text{ W m}^{-2}$, and $\sim 2 \text{ m s}^{-1}$,
451 respectively (Fig. 11b). The diurnal cycle in air temperature suggests that the boundary
452 layer is progressively warmed and destabilized by increasing SST, leading to a
453 progressive increase in wind speed as buoyancy-driven overturning amplifies. Around
454 14L, the sudden air temperature drop of $\sim 0.6^\circ\text{C}$ indicates the development of
455 evaporatively generated cold pools, which in turn provide a strong, albeit brief, boost to
456 air-sea fluxes (Figs. 10 and 11b). The composite evolution of SST and fluxes is
457 qualitatively similar during the Oct period, though with more limited diurnal variations
458 (Fig. 11a). The cloud response to this variation in air-sea fluxes, during *both* SP/MJO1
459 and SP/MJO2, was substantial (shown later).

460 To assess the organizational character of clouds in the DYNAMO array during the
461 MJO suppressed phases, sets of true-color images from the MODIS Aqua and Terra
462 satellites are provided (500-m resolution), with samples for SP/MJO1 (Fig. 12) and
463 SP/MJO2 (Fig. 13). The Aqua and Terra satellite overpass sequence provides closely
464 overlapping regional sampling each day, though with a three-hour gap between each
465 satellite’s overpass, thereby capturing the evolution of the sampled cloud scene (from the

466 late morning to the early afternoon). Since the overpasses shift each day, however, the
 467 sampling regions also shift. The images shown have been cropped from their originals
 468 with preference for regions nearest to the northern sounding array and away from image
 469 edges where information is distorted. The most prominent feature of these cloud scenes
 470 is the degree of mesoscale organization – virtually all clouds are part of either cloud
 471 streets (Figs. 12b,c, and 13h), indicative of horizontal convective rolls (HCRs;
 472 Weckwerth et al. 1996), or open cells (Figs. 12c–f and 13a,b, and d–f). The open cells
 473 range in diameter from roughly 15–50 km. While this organization fundamentally owes
 474 to heating from below by the warm ocean surface (i.e., Rayleigh–Bénard convection), the
 475 dimensionality of the organization relates to the dominance of shear- versus buoyancy-
 476 driven turbulent overturning.

477 The mode of this organization can be estimated from the ratio z_i/L , where z_i is the
 478 depth of convective overturning, and L the Obukhov length, given by

$$479 \quad L = -\frac{c_p \rho \theta_v u_*^3}{kgF_v}, \quad (6)$$

480 where ρ is density, θ_v virtual potential temperature, $u_* = \sqrt{\tau/\rho}$ friction velocity, k the
 481 von Kármán constant, $F_v = S_0 + 0.61c_pTE_0$ buoyancy flux, and τ shear stress at the
 482 surface. Weckwerth et al. (1999) suggest that HCRs are favored when $-z_i/L < 25$, i.e.,
 483 when low-level wind shear is relatively strong (or L relatively large), while cells are
 484 favored for larger ratio values, such as for relatively large surface buoyancy flux or weak
 485 wind speeds. Calculating L from (6) using *Revelle* flux site measurements, and taking z_i
 486 as mixed layer depth analyzed from *Revelle* soundings (Johnson et al. 2001), reveals
 487 mean ratio values of ~ 5 for the Oct suppressed period and ~ 130 for the Nov period.

488 Therefore, conditions generally favor HCRs in the Oct period and open cells in the Nov
489 period, owing to stronger low-level winds in SP/MJO1 relative to SP/MJO2, both from
490 the perspective of the Reville (Fig. 8) and the greater sounding array (Johnson and
491 Ciesielski 2013; their Fig. 12). While the role of evaporatively generated cold pools in
492 the observed organization is yet unclear, it is plausible that some of the cellular structures
493 depicted in Figs. 12 and 13 owe to outward-spreading cold pools, particularly late in the
494 suppressed phases as rainfall increases leading up to MJO onset (Figs. 2, 6, and 9–11)
495 (Rowe and Houze 2014). Detailed observations of the boundary layer thermodynamics
496 will be necessary to pin this down.

497 Weckwerth et al. (1996) show that the boundary layer circulation related to such
498 mesoscale organization augments the convective instability in the boundary layer by
499 creating localized areas of enhanced moisture, thereby leading to deeper convective
500 clouds than would otherwise occur. Therefore, the cloud organization depicted in Figs.
501 12 and 13 reflects the process by which mesoscale circulation enhances the
502 communication of moisture between the boundary layer and overlying free troposphere.

503 Also apparent during both suppressed periods is a slight change in the cloud
504 scenes within the three hours between satellite overpasses each day. Specifically, an
505 increase in the size and/or number of clouds suggests that moist convection is
506 intensifying. This change is particularly clear on 11, 12, and 14 Oct (Figs. 12c–h), and
507 11, 13, and 15 Nov (Figs. 13a,b, and e–h). Diurnal composites of echo-top frequency and
508 echo area coverage calculated from the S-Pol RHI dataset (cf. section 2) are shown for
509 segments of SP/MJO1 and SP/MJO2 in Fig. 14. During both suppressed periods, echo-
510 top frequency generally peaks in the lower troposphere, reflecting the dominance of

511 shallow cumuli, with echo area coverage ranging from 0~20%. An increase in low-level
512 echo-top frequency occurs, however, as echo area coverage begins to increase around
513 11L during the Oct period (Fig. 14a), and ~09L in the Nov period (Fig. 14b), followed by
514 a progressive deepening of echo tops thereafter. Frequency >0.5% reaches 9~11 km as
515 echo area peaks around 20% by 15L in both periods, indicating a midafternoon
516 population of congestus clouds with larger cloud size and/or quantity than earlier in the
517 day. These deeper clouds persist through evening in the Oct period, dissipating around
518 02L. During the Nov period, however, deep overnight convective clouds appear more
519 distinctly from afternoon convection, in both echo-top frequency and echo area coverage,
520 around 00~05L. This diurnal cycle in clouds occurs on a large scale (Figs. 12 and 13).

521 Diurnal composites of TRMM rainfall averaged over the northern sounding array
522 for the Nov and Oct periods are provided in Fig. 15. While the mean amounts are very
523 small, both periods exhibit increasing rainfall in the afternoon in connection with
524 deepening clouds and intensifying convection (Fig. 14). While rainfall in the Oct period
525 largely persists through night before tapering off in the morning (Fig. 15a), rainfall in the
526 Nov period exhibits a more distinct early-morning maximum offset by ~12 h from the
527 afternoon peak (Fig. 15b). This maximum in the Nov period is consistent with the
528 distinct early-morning maximum in echo-top frequency and echo coverage (Fig. 14),
529 though the timing is in slight disagreement. Differences in timing between Figs. 14 and
530 15 relate to differences in spatial sampling between S-Pol and the TRMM northern-array
531 average. The existence of both afternoon and nocturnal rainfall peaks was also observed
532 in COARE and MISMO (Sui et al. 1997; Johnson et al. 2001; Bellenger et al. 2010).

533 Figure 16 provides diurnal composite q , ω , Q_1 , and Q_2 derived from the
534 DYNAMO northern array gridded sounding analysis for the suppressed phases in Oct and
535 Nov. Specific humidity q is shown with composite mean removed (q'), though composite
536 means are retained in the other fields. There is marked consistency in the diurnal cycle
537 between the Oct and Nov suppressed phases. Both periods exhibit a morning–evening q'
538 swing of 0.4~0.6 g kg⁻¹ in the layer 900~550 hPa, with moister conditions in the evening.
539 Since temperature varies negligibly, this diurnal variation in q' directly correlates with
540 relative humidity, which exhibits anomalies of O(3%) (not shown). Most of the variation
541 in q' occurs below the 0°C level, reflecting the dominance of warm-rain clouds (Figs. 6
542 and 14). Anomalies of q' do appear above the 0°C level overnight, however, coinciding
543 with deeper clouds (Fig. 14). The diurnal variation in ω indicates enhanced deep
544 subsidence in the late evening–early morning, which likely relates to the remote forcing
545 of nocturnally invigorated deep convection in the ITCZ (this issue remains unsolved).
546 The weak rising motion (SP/MJO1; Fig. 16a) or relaxed subsidence (SP/MJO2; Fig. 16b)
547 in the lower troposphere in the morning–afternoon likely owes to the local increase in
548 convective heating. The evolution of Q_1 largely reflects the diurnal cycle of shortwave
549 heating, though enhanced warming near and within the boundary layer relates to the large
550 eddy flux of sensible heat from the surface as the mixed layer develops and deepens
551 (Johnson et al. 2001).

552 The diurnal cycle in Q_2 indicates pronounced daytime apparent moistening
553 peaking between 11~17L, which is in quadrature with q' , indicating the dominance of the
554 local tendency term in (2) (this was confirmed by a check of the individual contributions
555 to Q_2 ; not shown). Since $Q_2 < 0$ through most of the column (and precipitation is

556 negligible), this signal relates to the vertical convergence of vertical eddy moisture flux,
557 which ties to surface evaporation (2 and 4). This conclusion also follows by noting the
558 magnitude difference between Q_1 and Q_2 : if water phase changes dominated the moisture
559 source, Q_1 and Q_2 would exhibit similar magnitude (such as when there is heavy rainfall
560 in the active phase; Fig. 3). Therefore, while latent heat release in the cloud layer is
561 critical in driving convective eddies into the free troposphere, it is the large vertical eddy
562 moisture flux by the subgrid-scale circulation (i.e., convection within the mesoscale
563 circulations depicted in Figs. 12 and 13) that is driving this moistening. Q_2 moistening
564 reaches a peak of $\sim 10 \text{ K day}^{-1}$ at 14L around 800 hPa in the Oct period, which closely
565 coincides with the time of peak $L_v E_0$ as measured at the *Revelle* (Fig. 11; note the
566 difference in temporal resolution between these two datasets). While Q_2 moistening
567 persists within a shallow layer through much of the evening in SP/MJO1, Q_2 switches to
568 drying overnight–early morning during SP/MJO2. A cycle in q' and Q_2 also appears in
569 the boundary layer (i.e., below ~ 900 hPa), which is shifted slightly later than the cycle in
570 the free troposphere. While this boundary layer moistening is not yet understood, it has
571 been observed in previous field studies (Sui et al. 1997; Yasunaga et al. 2008). An issue
572 that remains unresolved is the role of water vapor storage in clouds: since the volume of
573 clouds exhibits substantial diurnal fluctuation (Fig. 14), the amount of water contained in
574 suspended hydrometeors likely also fluctuates (McNab and Betts 1978). This issue will
575 be the subject of a future study.

576 The findings described here demonstrate that the low-to-midlevel moistening
577 characteristic of the suppressed phase (or pre-onset stage) of the MJO is primarily driven
578 by the diurnal cycle of the convective cloud population. This diurnal cycle is

579 characterized by a daytime deepening of clouds from shallow to congestus, an increase in
580 their areal coverage, and a corresponding peak in cumulus moistening (Figs. 7 and 12–
581 16). The afternoon invigoration of convection is driven by the afternoon peak in SST and
582 air-sea fluxes, which owes to oceanic diurnal warm layers (Figs. 8–11) (Bellenger et al.
583 2010). A surprising finding is the prominence of mesoscale cloud organization during
584 the suppressed phase, which is manifest in HCRs and open cells, depending primarily on
585 the strength of the low-level wind (Figs. 12 and 13). This cloud organization is indicative
586 of buoyancy-driven boundary layer overturning circulation, which effectively assists the
587 communication of moisture between the boundary layer and the overlying free
588 troposphere (Weckwerth et al. 1996).

589

590 5. Summary and Conclusions

591 Atmospheric sounding, radar, and air-sea flux measurements collected during
592 DYNAMO are employed to diagnose the relationships between moist convection and the
593 large-scale environment during MJO initiation in the tropical Indian Ocean. This
594 diagnosis is carried out in two steps. First, an overview of the tropospheric moistening
595 processes is provided for the two DYNAMO MJO events via comparisons between the
596 apparent heating Q_1 and drying Q_2 , the column-integrated moisture budget, and cloud
597 measurements from radar (section 3). Provided second is a more detailed analysis of the
598 low-to-midlevel moistening that takes place leading up to MJO onset (i.e., the onset of
599 deep convection), highlighting the role of the diurnal cycle (section 4).

600 *A new finding of this study is that humidification of the troposphere during*
601 *MJO initiation occurs in a two-stage process: moistening of low–midlevels prior to*

602 *MJO onset, and of the full column in the early active phase.* These two stages are
603 distinguished by a switch in the key operative moistening agents at onset, as indicated by
604 the moisture budget (section 3). The main aspects of this two-stage moistening process
605 are summarized in Fig. 17a. During the suppressed phase, the moistening by non-
606 precipitating shallow cumulus clouds (via surface evaporation and vertical eddy moisture
607 flux) operates against the drying by large-scale circulation. Low-to-midlevel
608 humidification begins several days prior to MJO onset as subsidence and horizontal-
609 advective drying wane, thereby enabling the cloud population to effectively increase
610 column humidity. The abatement of large-scale subsidence and horizontal-advective
611 drying may be linked to an approaching Kelvin wave (Virts and Wallace 2010;
612 Gottschalck et al. 2013; Powell and Houze 2014; Sobel et al. 2014). Growth of the
613 convective cloud population continues as the low-to-midlevel moistening progresses,
614 leading to the eventual switch from apparent cooling and moistening to warming and
615 drying as widespread heavy rainfall begins, thus marking MJO onset. Deep-column
616 moistening is then facilitated in association with a bottom-heavy diabatic heating profile,
617 indicative of predominant congestus and cumulonimbus clouds, wherein the column
618 moisture source due to low-level convergence slightly exceeds the sink due to
619 precipitation (Wu 2003; Zhang et al. 2004; Chikira 2014). The convective cloud
620 population and associated diabatic heating continue to grow and amplify in close
621 correspondence with column moistening, until a switch to drying occurs with increasing
622 stratiform precipitation and dry-air advection in association with equatorial Rossby gyres
623 (Zipser 1977; Powell and Houze 2013; Kerns and Chen 2014; Rowe and Houze 2014;
624 Sobel et al. 2014).

625 While this two-stage moistening process is generally similar in the two
626 DYNAMO MJO events, the suppressed phase of the Nov MJO may be unique in that
627 much of the low-to-midlevel moistening occurs early in the suppressed phase, which is
628 separated by ~four days in which the column remains relatively humid up to ~550 hPa,
629 until moistening finally begins again late in the suppressed phase. This two-stage
630 moistening during the Oct MJO initiation event, in contrast, occurs in more continuous
631 fashion, and therefore more closely resembles the evolution depicted by prior studies
632 (e.g., Benedict and Randall 2007). It is difficult to be certain about the degree of
633 generality of these events, however, without observations of more MJO initiation events.

634 *A major new finding of this study is that the low-to-midlevel moistening*
635 *characteristic of the MJO suppressed phase (or pre-onset stage) is largely driven by the*
636 *diurnal cycle of clouds* (section 4). This diurnal cycle is characterized by a daytime
637 deepening and increase in the areal coverage of shallow cumuli, which develop into
638 congestus clouds by afternoon. This convective cloud growth drives a prominent
639 daytime maximum in cumulus moistening, which coincides with a peak in SST and air-
640 sea fluxes (Fig. 17b). This diurnal cycle in SST and air-sea fluxes is associated with
641 oceanic diurnal warm layers that form under light-wind, clear-sky conditions (Halpern
642 and Reed 1976; Bellenger et al. 2010). Not analyzed herein is the two-day variability
643 observed in the active phase of the Oct MJO event (Fig. 6), which is linked to westward-
644 moving waves studied previously (Haertel et al. 2008; Zuluaga and Houze 2013). It is
645 possible that the local diurnal cycle and this two-day cycle are linked (e.g., Chen and
646 Houze 1997), though further study is necessary to pin this down.

647 *A conspicuous finding of this study is the prominence of mesoscale cloud*
648 *organization observed during the suppressed phase, which is manifest in open cells and*
649 *horizontal convective rolls* (Fig. 17c). The character of this organization relates to the
650 relative magnitudes of shear-driven and buoyancy-driven turbulence, though it
651 fundamentally owes to heating from below by the warm ocean surface. More work is
652 needed to ascertain the role of cold pools in the observed organization.

653 The above two new findings pertaining to the MJO suppressed phase lead to two
654 new hypotheses tied to the moisture preconditioning during this stage of the MJO:

- 655 1. *The daytime peak in sea surface temperature and air-sea fluxes and the*
656 *resulting boost to convective activity cause more vigorous tropospheric*
657 *moistening than would occur without such a diurnal cycle.*
- 658 2. *The mesoscale organization of clouds and the associated subgrid-scale*
659 *overturning circulation lead to localized patches of enhanced boundary layer*
660 *moisture and deeper mixed layers* (Weckwerth et al. 1996; Johnson et al. 2001),
661 *which promote deeper clouds and more vigorous moistening than would*
662 *otherwise occur.*

663 Proper testing of these hypotheses using models will require, at minimum, simultaneous
664 resolution of both the cumulus scale, of $O(\leq 500 \text{ m})$, and the mesoscale cloud
665 organization, of $O(10\text{--}100 \text{ km})$ (Figs. 12 and 13).

666 Recent modeling studies demonstrate that the tropical oceanic diurnal cycle,
667 wherein the heat received during the day in the shallow warm layer is convectively mixed
668 downwards overnight, is crucial to rectifying the slow (i.e., intraseasonal) SST increase
669 during the suppressed phase of the MJO (Webster et al. 1996; Duvel et al. 2004; Bernie et

670 al. 2005, 2008; Vialard et al. 2009). While it is yet unclear if and how this *intraseasonal*
671 SST increase directly links to MJO onset, it is plausible that this *diurnal cycle* in SST,
672 and the diurnal cycle that it drives in clouds, is key to rectifying the cumulus moistening
673 that occurs on the MJO timescale leading up to MJO onset. This possible link, which
674 underpins Hypothesis 1 above, has major implications for modeling of the MJO.

675

676 *Acknowledgments.*

677 We thank Paul Ciesielski (Colorado State University; CSU) for the processing of
678 the DYNAMO sounding dataset, Zhe Feng (ARM–Pacific Northwest National
679 Laboratory) and the Robert Houze research group (University of Washington) for their
680 efforts with the S-Pol dataset, and Jim Edson (University of Connecticut), Chris Fairall
681 (Earth System Research Laboratory Physical Sciences Division), and Simon De Szoeki
682 (Oregon State University) for their efforts with the air–sea flux dataset. We acknowledge
683 many colleagues for inspiring discussions of this work, especially Paul Ciesielski,
684 Charlotte DeMott, Alex Gonzalez, Walter Hannah, Elizabeth Thompson, and Brandon
685 Wolding from CSU. Chidong Zhang (University of Miami) and all other participants in
686 DYNAMO/CINDY/AMIE/LASP are greatly acknowledged. This research has been
687 supported by the National Science Foundation under Grants AGS-1059899, AGS-
688 1138353, and AGS-1360237, the National Aeronautics and Space Administration under
689 Grant NNX13AF74G, and the Department of Energy Grant DE-SC0008582.

690

691 **References**

- 692 Arakawa, A., and W. H. Schubert, 1974: Interaction of a cumulus cloud ensemble with
693 the large-scale environment, Part I. *J. Atmos. Sci.*, **31**, 674–701.
- 694 Austin, J. M., 1948: A note on cumulus growth in a nonsaturated environment. *J.*
695 *Meteor.*, **5**, 103–107.
- 696 Bellenger, H., Y. N. Takayabu, T. Ushiyama, and K. Yoneyama, 2010: Role of diurnal
697 warm layers in the diurnal cycle of convection over the tropical Indian Ocean during
698 MISMO. *Mon. Wea. Rev.*, **138**, 2426–2433.
- 699 Benedict, J. J., and D. A. Randall, 2007: Observed characteristics of the MJO relative to
700 maximum rainfall. *J. Atmos. Sci.*, **64**, 2332–2354.
- 701 Bernie, D. J., S. J. Woolnough, J. M. Slingo, and E. Guilyardi, 2005: Modeling diurnal
702 and intraseasonal variability of the ocean mixed layer. *J. Clim.*, **18**, 1190–1202.
- 703 ———, E. Guilyardi, G. Madec, J. M. Slingo, S. J. Woolnough, and J. Cole, 2008: Impact
704 of resolving the diurnal cycle in an ocean–atmosphere GCM. Part 2: A diurnally
705 coupled CGCM. *Clim. Dyn.*, **31**, 909–925.
- 706 Bladé, I., and D. L. Hartmann, 1993: Tropical intraseasonal oscillations in a simple
707 nonlinear model. *J. Atmos. Sci.*, **50**, 2922–2939.
- 708 Chen, S. S., and R. A. Houze, Jr., 1997: Diurnal variation and life-cycle of deep
709 convective systems over the tropical Pacific warm pool. *Quart. J. Roy. Meteor. Soc.*,
710 **123**, 357–388.
- 711 ———, ———, and B. E. Mapes, 1996: Multiscale variability of deep convection in relation
712 to large-scale circulation in TOGA COARE. *J. Atmos. Sci.*, **53**, 1380–1409.
- 713 Chikira, M., 2014: Eastward-propagating intraseasonal oscillation represented by
714 Chikira–Sugiyama cumulus parameterization. Part II: Understanding moisture
715 variation under weak temperature gradient balance. *J. Atmos. Sci.*, **71**, 615–639.
- 716 Ciesielski, P. E., R. H. Johnson, P. T. Haertel, and J. Wang, 2003: Corrected TOGA
717 COARE sounding humidity data: Impact on diagnosed properties of convection and
718 climate over the warm pool. *J. Climate*, **16**, 2370–2384.
- 719 ———, and Coauthors, 2014a: Quality-controlled upper-air sounding dataset for
720 DYNAMO/CINDY/AMIE: Development and corrections. *J. Atmos. Oceanic*
721 *Technol.*, **31**, 741–764.
- 722 ———, R. H. Johnson, K. Yoneyama, and R. K. Taft, 2014b: Mitigation of Sri Lanka
723 island effects in Colombo sounding data and its impact on DYNAMO analyses. *J.*
724 *Meteor. Soc. Japan*, accepted.

- 725 Dai, A., 2001: Global precipitation and thunderstorm frequencies. Part II: Diurnal
726 variations. *J. Climate*, **14**, 1112–1128.
- 727 Davison, J. L., R. M. Rauber, and L. Di Girolamo, 2013: A revised conceptual model of
728 the tropical marine boundary layer. Part II: Detecting relative humidity layers using
729 Bragg scattering from S-Band radar. *J. Atmos. Sci.*, **70**, 3025–3046.
- 730 DeMott, C. A., and S. A. Rutledge, 1998: The Vertical Structure of TOGA COARE Th
731 vertical structure of TOGA COARE convection. Part II: Modulating influences and
732 implications for diabatic heating. *J. Atmos. Sci.*, **55**, 2748–2762.
- 733 Duvel, J. P., R. Roca, and J. Vialard, 2004: Ocean mixed layer temperature variations
734 induced by intraseasonal convective perturbations over the Indian Ocean. *J. Atmos.*
735 *Sci.*, **61**, 1004–1023.
- 736 Feng, Z., S. A. McFarlane, C. Schumacher, S. Ellis, J. Comstock, and N. Bharadwaj,
737 2014: Constructing a merged cloud–precipitation radar dataset for tropical convective
738 clouds during the DYNAMO/AMIE experiment at Addu Atoll. *J. Atmos. Oceanic*
739 *Technol.*, **31**, 1021–1042.
- 740 Flament, P., J. Firing, M. Sawyer, and C. Trefois, 1994: Amplitude and horizontal
741 structure of a large diurnal sea surface warming event during the Coastal Ocean
742 Dynamics Experiment. *J. Phys. Oceanogr.*, **24**, 124–139.
- 743 Del Genio, A. D., Y. Chen, D. Kim, and M.-S. Yao, 2012: The MJO transition from
744 shallow to deep convection in CloudSat/CALIPSO data and GISS GCM simulations.
745 *J. Climate*, **25**, 3755–3770.
- 746 Gill, A. E., 1980: Some simple solutions for heat-induced tropical circulation. *Quart. J.*
747 *Roy. Meteor. Soc.*, **106**, 447–462.
- 748 Gottschalck, J., P. E. Roundy, C. J. Schreck III, A. Vintzileos, and C. Zhang, 2013:
749 Large-scale atmospheric and oceanic conditions during the 2011–12 DYNAMO field
750 campaign. *Mon. Wea. Rev.*, **141**, 4173–4196.
- 751 Gray, W. M., and R. W. Jacobson, 1977: Diurnal variation of deep cumulus convection.
752 *Mon. Wea. Rev.*, **105**, 1171–1188.
- 753 Haertel, P. T., G. N. Kiladis, A. Denno, and T. M. Rickenbach, 2008: Vertical-mode
754 decompositions of 2-day waves and the Madden–Julian oscillation. *J. Atmos. Sci.*, **65**,
755 813–833.
- 756 Halpern, D., and R. K. Reed, 1976: Heat budget of the upper ocean under light winds. *J.*
757 *Phys. Oceanogr.*, **6**, 972–975.
- 758 Hannah, W. M., and E. D. Maloney, 2011: The role of moisture–convection feedbacks in
759 simulating the Madden–Julian oscillation. *J. Climate*, **24**, 2754–2770.

- 760 Hendon, H. H., and B. Liebmann, 1990: The intraseasonal (30–50 day) oscillation of the
761 Australian summer monsoon. *J. Atmos. Sci.*, **47**, 2909–2924.
- 762 ———, and M. L. Salby, 1994: The life cycle of the Madden–Julian oscillation. *J. Atmos.*
763 *Sci.*, **51**, 2225–2237.
- 764 ———, B. Liebmann, M. Newman, J. D. Glick, and J. E. Schemm, 2000: Medium-range
765 forecast errors associated with active episodes of the Madden-Julian oscillation. *Mon.*
766 *Wea. Rev.*, **128**, 69–86.
- 767 Holloway, C. E., and J. D. Neelin, 2009: Moisture vertical structure, column water vapor,
768 and tropical deep convection. *J. Atmos. Sci.*, **66**, 1665–1683.
- 769 Hu, Q., and D. A. Randall, 1994: Low-frequency oscillations in radiative-convective
770 systems. *J. Atmos. Sci.*, **51**, 1089–1099.
- 771 Huffman, G. J., R. F. Adler, D. T. Bolvin, G. Gu, E. J. Nelkin, K. P. Bowman, E. F.
772 Stocker, and D. B. Wolff, 2007: The TRMM Multisatellite Precipitation Analysis
773 (TMPA): Quasi-global, multiyear, combined-sensor precipitation estimates at fine
774 scales. *J. Hydrometeor.*, **8**, 38–55.
- 775 Jiang, X., and Coauthors, 2011: Vertical diabatic heating structure of the MJO:
776 Intercomparison between recent reanalyses and TRMM estimates. *Mon. Wea. Rev.*,
777 **139**, 3208–3223.
- 778 Johnson, R. H., 2011: Diurnal cycle of monsoon convection. *The Global Monsoon*
779 *System: Research and Forecasts*, 2nd ed. C.-P. Chang et al., Eds., World Scientific,
780 257–276.
- 781 ———, and X. Lin, 1997: Episodic trade wind regimes over the western Pacific warm pool.
782 *J. Atmos. Sci.*, **54**, 2020–2034.
- 783 ———, and P. E. Ciesielski, 2002: Characteristics of the 1998 summer monsoon onset over
784 the northern South China Sea. *J. Meteor. Soc. Japan*, **80**, 561–578.
- 785 ———, and ———, 2013: Structure and properties of Madden–Julian oscillations deduced
786 from DYNAMO sounding arrays. *J. Atmos. Sci.*, **70**, 3157–3179.
- 787 ———, ———, and J. A. Cotturone, 2001: Multiscale variability of the atmospheric mixed
788 layer over the western Pacific warm pool. *J. Atmos. Sci.*, **58**, 2729–2750.
- 789 ———, ———, T. S. L’Ecuyer, and A. J. Newman, 2010: Diurnal cycle of convection during
790 the 2004 North American Monsoon Experiment. *J. Climate*, **23**, 1060–1078.
- 791 ———, ———, J. H. Ruppert, Jr., and M. Katsumata, 2014: Sounding-based thermodynamic
792 budgets for DYNAMO. *J. Atmos. Sci.*, submitted.

- 793 ———, T. M. Rickenbach, S. A. Rutledge, P. E. Ciesielski, and W. H. Schubert, 1999:
794 Trimodal characteristics of tropical convection. *J. Climate*, **12**, 2397–2418.
- 795 Katsumata, M., P. E. Ciesielski, and R. H. Johnson, 2011: Evaluation of budget analyses
796 during MISMO. *J. Appl. Meteor. Climatol.*, **50**, 241–254.
- 797 Kawai, Y., and A. Wada, 2007: Diurnal sea surface temperature variation and Its Impact
798 on the atmosphere and ocean: A review. *J. Oceanogr.*, **63**, 721–744.
- 799 Keeler, R. J., J. Lutz, and J. Vivekanandan, 2000: S-Pol: NCAR’s polarimetric Doppler
800 research radar. IGARS 2000: IEEE 2000 International Geoscience and Remote
801 Sensing Symposium, T. I. Stein, Ed., Vol. 4, 1570–1573,
802 doi:10.1109/IGARSS.2000.857275.
- 803 Kerns, B. W., and S. S. Chen, 2014: Equatorial dry air intrusion and related synoptic
804 variability in MJO initiation during DYNAMO. *Mon. Wea. Rev.*, **142**, 1326–1343.
- 805 Kikuchi, K., and Y. N. Takayabu, 2004: The development of organized convection
806 associated with the MJO during TOGA COARE IOP: Trimodal characteristics.
807 *Geophys. Res. Lett.*, **31**, L10101.
- 808 Kiladis, G. N., K. H. Straub, and P. T. Haertel, 2005: Zonal and vertical structure of the
809 Madden-Julian oscillation. *J. Atmos. Sci.*, **62**, 2790–2809.
- 810 ———, K. H. Straub, G. C. Reid, and K. S. Gage, 2001: Aspects of interannual and
811 intraseasonal variability of the tropopause and lower stratosphere. *Quart. J. Roy.
812 Meteor. Soc.*, **127**, 1961–1983.
- 813 Kummerow, C., and Coauthors, 2000: The status of the Tropical Rainfall Measuring
814 Mission (TRMM) after two years in orbit. *J. Appl. Meteor.*, **39**, 1965–1982.
- 815 Lin, J. L., and G. N. Kiladis, 2006: Tropical intraseasonal variability in 14 IPCC AR4
816 climate models. Part I: Convective signals. *J. Climate*, **19**, 2665–2690.
- 817 Lin, X., and R. H. Johnson, 1996a: Kinematic and thermodynamic characteristics of the
818 flow over the western Pacific warm pool during TOGA COARE. *J. Atmos. Sci.*, **53**,
819 695–715.
- 820 ———, and ———, 1996b: Heating, moistening, and rainfall over the western Pacific warm
821 pool during TOGA COARE. *J. Atmos. Sci.*, **53**, 3367–3383.
- 822 Liu, C., E. J. Zipser, and S. W. Nesbitt, 2007: Global distribution of tropical deep
823 convection: Different perspectives from TRMM infrared and radar data. *J. Climate*,
824 **20**, 489–503.
- 825 Madden, R. A., and P. R. Julian, 1971: Detection of a 40-50 day oscillation in the zonal
826 wind in the tropical Pacific. *J. Atmos. Sci.*, **28**, 702–708.

- 827 ———, and ———, 1972: Description of global-scale circulation cells in the tropics with a
828 40–50 day period. *J. Atmos. Sci.*, **29**, 1109–1123.
- 829 Majda, A. J., and S. N. Stechmann, 2009: The skeleton of tropical intraseasonal
830 oscillations. *Proc. Natl. Acad. Sci. USA*, **106**, 8417–8422.
- 831 Maloney, E. D., 2009: The moist static energy budget of a composite tropical
832 intraseasonal oscillation in a climate model. *J. Climate*, **22**, 711–729.
- 833 ———, and D. L. Hartmann, 1998: Frictional moisture convergence in a composite life
834 cycle of the Madden-Julian oscillation. *J. Climate*, **11**, 2387–2403.
- 835 ———, A. H. Sobel, and W. M. Hannah, 2010: Intraseasonal variability in an aquaplanet
836 general circulation model. *J. Adv. Model. Earth Sys.*, **2**, 1–24.
- 837 Mapes, B. E., and P. Zuidema, 1996: Radiative-dynamical consequences of dry tongues
838 in the tropical troposphere. *J. Atmos. Sci.*, **53**, 620–638.
- 839 ———, P. E. Ciesielski, and R. H. Johnson, 2003: Sampling errors in rawinsonde-array
840 budgets. *J. Atmos. Sci.*, **60**, 2697–2714.
- 841 ———, S. Tulich, J. Lin, and P. Zuidema, 2006: The mesoscale convection life cycle:
842 Building block or prototype for large-scale tropical waves? *Dyn. Atmos. Ocean.*, **42**,
843 3–29.
- 844 Matsuno, T. 1966: Quasi-geostrophic motions in the equatorial area. *J. Meteor. Soc.
845 Japan*, **44**, 25–43.
- 846 McNab, A. L., and A. K. Betts, 1978: A mesoscale budget study of cumulus convection.
847 *Mon. Wea. Rev.*, **106**, 1317–1331.
- 848 Moncrieff, M. W., D. E. Waliser, M. J. Miller, M. a. Shapiro, G. R. Asrar, and J.
849 Caughey, 2012: Multiscale convective organization and the YOTC virtual global field
850 campaign. *Bull. Amer. Meteor. Soc.*, **93**, 1171–1187.
- 851 Neelin, J. D., and I. M. Held, 1987: Modeling tropical convergence based on the moist
852 static energy budget. *Mon. Wea. Rev.*, **115**, 3–12.
- 853 Nitta, T., and S. Esbensen, 1974: Heat and moisture budget analyses using BOMEX data.
854 *Mon. Wea. Rev.*, **102**, 17–28.
- 855 Nuss, W. A., and D. W. Titley, 1994: Use of multiquadric interpolation for
856 meteorological objective analysis. *Mon. Wea. Rev.*, **122**, 1611–1631.
- 857 Powell, S. W., and R. A. Houze, 2013: The cloud population and onset of the Madden-
858 Julian oscillation over the Indian Ocean during DYNAMO-AMIE. *J. Geophys. Res.*,
859 **118**, 11 979–11 995.

- 860 —, and R. A. Houze, Jr., 2014: Eastward propagating upper-tropospheric zonal wind
861 and temperature anomalies moving over the equatorial Indian Ocean and their
862 relations to MJO convective onset. *J. Geophys. Res.*, submitted.
- 863 Praveen Kumar, B., J. Vialard, M. Lengaigne, V. S. N. Murty, and M. J. McPhaden,
864 2011: TropFlux: air-sea fluxes for the global tropical oceans—description and
865 evaluation. *Clim. Dyn.*, **38**, 1521–1543.
- 866 Randall, D. A., Harshvardhan, and D. A. Dazlich, 1991: Diurnal variability of the
867 hydrologic cycle in a general circulation model. *J. Atmos. Sci.*, **48**, 40–62.
- 868 Raymond, D. J., 2001: A new model of the Madden–Julian oscillation. *J. Atmos. Sci.*, **58**,
869 2807–2819.
- 870 —, and Ž. Fuchs, 2009: Moisture modes and the Madden–Julian oscillation. *J.*
871 *Climate*, **22**, 3031–3046.
- 872 —, S. L. Sessions, A. H. Sobel, and Ž. Fuchs, 2009: The mechanics of gross moist
873 stability. *J. Adv. Model. Earth Sys.*, **1**, 1–20.
- 874 Redelsperger, J. L., D. B. Parsons, and F. Guichard, 2002: Recovery processes and
875 factors limiting cloud-top height following the arrival of a dry intrusion observed
876 during TOGA COARE. *J. Atmos. Sci.*, **59**, 2438–2457.
- 877 Riley, E. M., B. E. Mapes, and S. N. Tulich, 2011: Clouds associated with the Madden–
878 Julian oscillation: A new perspective from CloudSat. *J. Atmos. Sci.*, **68**, 3032–3051.
- 879 Rowe, A. K., and R. A. Houze, 2014: Microphysical characteristics of MJO convection
880 over the Indian Ocean during DYNAMO. *J. Geophys. Res.*, **119**, 2543–2554.
- 881 Rui, H., and B. Wang, 1990: Development characteristics and dynamic structure of
882 tropical intraseasonal convection anomalies. *J. Atmos. Sci.*, **47**, 357–379.
- 883 Ruppert, J. H., Jr., R. H. Johnson, and A. K. Rowe, 2013: Diurnal circulations and
884 rainfall in Taiwan during SoWMEX/TiMREX (2008). *Mon. Wea. Rev.*, **141**, 3851–
885 3872.
- 886 Sobel, A., and E. Maloney, 2013: Moisture modes and the eastward propagation of the
887 MJO. *J. Atmos. Sci.*, **70**, 187–192.
- 888 —, J. Nilsson, and L. M. Polvani, 2001: The weak temperature gradient approximation
889 and balanced tropical moisture waves. *J. Atmos. Sci.*, **58**, 3650–3665.
- 890 —, S. Wang, and D. Kim, 2014: Moist static energy budget of the MJO during
891 DYNAMO. *J. Atmos. Sci.*, submitted.
- 892 —, S. E. Yuter, C. S. Bretherton, and G. N. Kiladis, 2004: Large-scale meteorology
893 and deep convection during TRMM KWAJEX. *Mon. Wea. Rev.*, **132**, 422–444.

- 894 Stephens, G. L., P. J. Webster, R. H. Johnson, R. Engelen, and T. L'Ecuyer, 2004:
895 Observational evidence for the mutual regulation of the tropical hydrological cycle
896 and tropical sea surface temperatures. *J. Climate*, **17**, 2213–2224.
- 897 Stramma, L., P. Cornillon, R. A. Weller, J. F. Price, and M. G. Briscoe, 1986: Large
898 diurnal sea surface temperature variability: Satellite and in situ measurements. *J.*
899 *Phys. Oceanogr.*, **16**, 827–837.
- 900 Sui, C.-H., K.-M. Lau, Y. N. Takayabu, and D. A. Short, 1997: Diurnal variations in
901 tropical oceanic cumulus convection during TOGA COARE. *J. Atmos. Sci.*, **54**, 639–
902 655.
- 903 ———, X. Li, and K.-M. Lau, 1998: Radiative-convective processes in simulated diurnal
904 variations of tropical oceanic convection. *J. Atmos. Sci.*, **55**, 2345–2357.
- 905 Takemi, T., O. Hirayama, and C. Liu, 2004: Factors responsible for the vertical
906 development of tropical oceanic cumulus convection. *Geophys. Res. Lett.*, **31**,
907 L11109.
- 908 Vialard, J., and Coauthors, 2009: CIRENE: Air—sea interactions in the Seychelles—
909 Chagos thermocline ridge region. *Bull. Amer. Meteor. Soc.*, **90**, 45–61.
- 910 Virts, K. S., and J. M. Wallace, 2010: Annual, interannual, and intraseasonal variability
911 of tropical tropopause transition layer cirrus. *J. Atmos. Sci.*, **67**, 3097–3112.
- 912 ———, J. M. Wallace, Q. Fu, and T. P. Ackerman, 2010: Tropical tropopause transition
913 layer cirrus as represented by CALIPSO lidar observations. *J. Atmos. Sci.*, **67**, 3113–
914 3129.
- 915 Waite, M. L., and B. Khouider, 2010: The deepening of tropical convection by congestus
916 preconditioning. *J. Atmos. Sci.*, **67**, 2601–2615.
- 917 Waliser, D. E., K. M. Lau, W. Stern, and C. Jones, 2003: Potential predictability of the
918 Madden–Julian oscillation. *Bull. Amer. Meteor. Soc.*, **84**, 33–50.
- 919 ———, and Coauthors, 2012: The “Year” of Tropical Convection (May 2008–April 2010):
920 Climate variability and weather highlights. *Bull. Amer. Meteor. Soc.*, **93**, 1189–1218.
- 921 Webster, P. J., C. A. Clayson, and J. A. Curry, 1996: Clouds, radiation, and the diurnal
922 cycle of sea surface temperature in the tropical western Pacific. *J. Climate*, **9**, 1712–
923 1730.
- 924 Weckwerth, T. M., J. W. Wilson, and R. M. Wakimoto, 1996: Thermodynamic
925 variability within the convective boundary layer due to horizontal convective rolls.
926 *Mon. Wea. Rev.*, **124**, 769–784.
- 927 ———, T. W. Horst, and J. W. Wilson, 1999: An observational study of the evolution of
928 horizontal convective rolls. *Mon. Wea. Rev.*, **127**, 2160–2179.

- 929 Wei, D., A. M. Blyth, and D. J. Raymond, 1998: Buoyancy of convective clouds in
930 TOGA COARE. *J. Atmos. Sci.*, **55**, 3381–3391.
- 931 Weller, R. A., and S. P. Anderson, 1996: Surface meteorology and air-sea fluxes in the
932 western equatorial Pacific warm pool during the TOGA Coupled Ocean-Atmosphere
933 Response Experiment. *J. Climate*, **9**, 1959–1990.
- 934 Wheeler, M. C., and H. H. Hendon, 2004: An all-season real-time multivariate MJO
935 index: Development of an index for monitoring and prediction. *Mon. Wea. Rev.*, **132**,
936 1917–1932.
- 937 Wu, Z., 2003: A shallow CISK, deep equilibrium mechanism for the interaction between
938 large-scale convection and large-scale circulations in the tropics. *J. Atmos. Sci.*, **60**,
939 377–392.
- 940 Xu, K.-M., and D. A. Randall, 1995: Impact of interactive radiative transfer on the
941 macroscopic behavior of cumulus ensembles. Part II: Mechanisms for cloud-radiation
942 interactions. *J. Atmos. Sci.*, **52**, 800–817.
- 943 Yanai, M., and R. H. Johnson, 1993: Impacts of cumulus convection on thermodynamic
944 fields. *Meteor. Monogr.*, **24**, 39–62.
- 945 ———, S. Esbensen, and J.-H. Chu, 1973: Determination of bulk properties of tropical
946 cloud clusters from large-scale heat and moisture budgets. *J. Atmos. Sci.*, **30**, 611–
947 627.
- 948 Yang, S., and E. A. Smith, 2006: Mechanisms for diurnal variability of global tropical
949 rainfall observed from TRMM. *J. Climate*, **19**, 5190–5226.
- 950 Yasunaga, K., M. Fujita, T. Ushiyama, K. Yoneyama, Y. N. Takayabu, and M.
951 Yoshizaki, 2008: Diurnal variations in precipitable water observed by shipborne GPS
952 over the tropical Indian Ocean. *SOLA*, **4**, 97–100.
- 953 Yoneyama, K., C. Zhang, and C. N. Long, 2013: Tracking pulses of the Madden–Julian
954 oscillation. *Bull. Amer. Meteor. Soc.*, **94**, 1871–1891.
- 955 ———, and Coauthors, 2008: Mismo field experiment in the equatorial Indian Ocean. *Bull.*
956 *Amer. Meteor. Soc.*, **89**, 1889–1903.
- 957 Yu, J.-Y., C. Chou, and J. D. Neelin, 1998: Estimating the gross moist stability of the
958 tropical atmosphere. *J. Atmos. Sci.*, **55**, 1354–1372.
- 959 Zhang, C., 2005: Madden-Julian oscillation. *Rev. Geophys.*, **43**, RG2003.
- 960 ———, 2013: Madden-Julian Oscillation: Bridging weather and climate. *Bull. Amer.*
961 *Meteor. Soc.*, **94**, 1849–1870.

- 962 ———, M. McGauley, and N. Bond, 2004: Shallow meridional circulation in the tropical
963 eastern Pacific. *J. Climate*, 133–139.
- 964 ———, J. Gottschalck, E. D. Maloney, M. W. Moncrieff, F. Vitart, D. E. Waliser, B.
965 Wang, and M. C. Wheeler, 2013: Cracking the MJO nut. *Geophys. Res. Lett.*, **40**,
966 1223–1230.
- 967 Zipser, E. J., 1977: Mesoscale and convective-scale downdrafts as distinct components of
968 squall-line structure. *Mon. Wea. Rev.*, **105**, 1568–1589.
- 969 Zuluaga, M. D., and R. A. Houze, 2013: Evolution of the population of precipitating
970 convective systems over the equatorial Indian Ocean in active phases of the Madden–
971 Julian oscillation. *J. Atmos. Sci.*, **70**, 2713–2725.
- 972

973 **List of Figures**

974 FIG. 1. DYNAMO northern sounding array for the period October–December 2011.
 975 Soundings were launched four–eight times per day, as indicated. Locations of the NCAR
 976 S-Pol radar (Addu Atoll) and air-sea flux site (R/V *Revelle*) are also indicated.

977 FIG. 2. (top) Time–pressure series of daily-mean relative humidity RH (%; with respect to
 978 ice where temperature $< 0^{\circ}\text{C}$) from the northern-array gridded analysis spanning the Oct
 979 and Nov MJO events (MJO1 and MJO2, respectively). (bottom) Daily-mean rainfall
 980 estimates (mm day^{-1}) from TRMM 3B42 (solid) and the moisture budget (4) P_0 (dashed).
 981 Both fields have been temporally smoothed using a three-day running mean. Correlation
 982 r between the smoothed rainfall estimates is indicated (significant to the 99% level using
 983 the Student’s t-test and assuming a sample size of seven, the approximate number of ten-
 984 day periods in the dataset). Here and in subsequent figures: “SP” refers to suppressed
 985 periods, and “BH” (“TH”) to periods of bottom-heavy (top-heavy) apparent heating,
 986 drying, and vertical motion profiles (Figs. 3 and 4) (see text for date ranges); the black
 987 “X” along the abscissa indicates periods when the *Revelle* made a port call; and the
 988 vertical lines denote MJO onset (i.e., when the apparent cooling and moistening switch to
 989 heating and drying).

990 FIG. 3. Daily-mean time–pressure series of the apparent heat source Q_1 (top) and apparent
 991 moisture sink Q_2 (bottom) (K day^{-1}). The zero contour is dashed. Three-day temporal
 992 smoothing has been applied.

993 FIG. 4. As in Fig. 3 except for vertical pressure velocity ω (hPa day^{-1}). X’s are placed in
 994 several places to highlight the shift of the level of maximum ascent.

995 FIG. 5. (top) Daily-mean vertically integrated water vapor budget (10^2 W m^{-2}) and
 996 (bottom) P_0 (mm day^{-1}). Budget terms are calculated as shown in (5), with the local
 997 tendency (black), horizontal advection (red, dot-dashed), vertical advection (red, dotted),
 998 the sum of horizontal and vertical advection (SUM(ADV); red, solid), and apparent
 999 sources (green). Maximum and minimum values for terms exceeding the ordinate scale
 1000 are indicated (top). Five-day temporal smoothing has been applied to all fields.

1001 FIG. 6. Time–height series of echo-top frequency and echo area coverage (%) from 15-
 1002 min S-Pol RHI data. Temporal smoothing has been applied to echo-top frequency (echo
 1003 area coverage) using a six-hour (five-day) running mean. Black hashes near the top
 1004 indicate time periods of missing data (where the time gap between scans exceeded 23
 1005 min). The dashed line indicates the 0°C level.

1006 FIG. 7. Time–pressure series of Q_2 (K day^{-1}) for the suppressed and early-active phases of
 1007 (top) MJO1 and (bottom) MJO2. The dotted vertical lines mark local noon. Three-point
 1008 smoothing has been applied in the vertical (i.e., over 50 hPa) and in time (i.e., over six
 1009 hours).

1010 FIG. 8. Time series of sea surface temperature (SST, adjusted to skin temperature; black;
 1011 °C; left axis), SST smoothed using a 24-h running mean ($\text{SST}_{\text{daily}}$; blue), and surface
 1012 wind speed smoothed using a 24-h running mean (red; m s^{-1} ; right axis) from the *Revelle*
 1013 flux site. All fields from the *Revelle* flux site originate from 10-min data.

1014 FIG. 9. (top) Time series spanning the suppressed phase of MJO1 with SST (black; °C;
 1015 left axis), 10-m air temperature (green; °C; outer-right axis), and surface sensible heat
 1016 flux S_0 (red; W m^{-2} ; inner-right axis) from the *Revelle* (red; W m^{-2} ; right axis). (bottom)
 1017 As in the top except with wind speed (black; m s^{-1} ; left axis) and surface latent heat flux
 1018 $L_v E_0$ (red; W m^{-2} ; right axis). S_0 and $L_v E_0$ have been smoothed using a one-hour running
 1019 mean.

1020 FIG. 10. As in Fig. 9 except for the suppressed phase of MJO2.

1021 FIG. 11. (top) Diurnal composite SST (black; °C; left axis), 10-m air temperature (green;
 1022 °C; left axis), and S_0 (red; W m^{-2} ; right axis) for the (a) Oct (MJO1) and (b) Nov (MJO2)
 1023 suppressed phases. Composite means have been removed. (bottom) As in the top except
 1024 with wind speed (black; m s^{-1} ; left axis) and surface latent heat flux $L_v E_0$ (red; W m^{-2} ;
 1025 right axis). Composite date ranges are (a) 6–11 Oct and (b) 13–16 Nov (end-dates are
 1026 inclusive). Local time is indicated along the abscissa. Vertical dashed lines indicate
 1027 local noon. All fields have been smoothed using a 30-min running mean.

1028 FIG. 12. Cropped true-color images from the Terra (left) and Aqua (right) MODIS
 1029 satellites for selected dates of the Oct suppressed phase (MJO1). Date is indicated in the
 1030 left column, and UTC and local time are indicated in each panel. The magenta star marks
 1031 Huvadhu Atoll, located ~100 km north of Addu Atoll. Red and blue arrows indicate
 1032 subjectively identified corresponding cloud features between same-day images.

1033 FIG. 13. As in Fig. 11 except for the Nov suppressed phase (MJO2).

1034 FIG. 14. Diurnal time–height composites of convective echo-top frequency and echo area
 1035 coverage (%) for the (a) Oct and (b) Nov suppressed phases, calculated from 15-min S-
 1036 Pol RHI data. Composite date ranges are (a) 7–13 Oct and (b) 13–16 Nov (end-dates are
 1037 inclusive). Local time is indicated along the abscissa. Asterisks mark the time of
 1038 increasing echo-top frequency and echo area coverage. The 11- and 9-km levels are
 1039 indicated by dotted lines. Horizontal dashed lines indicate the 0°C level.

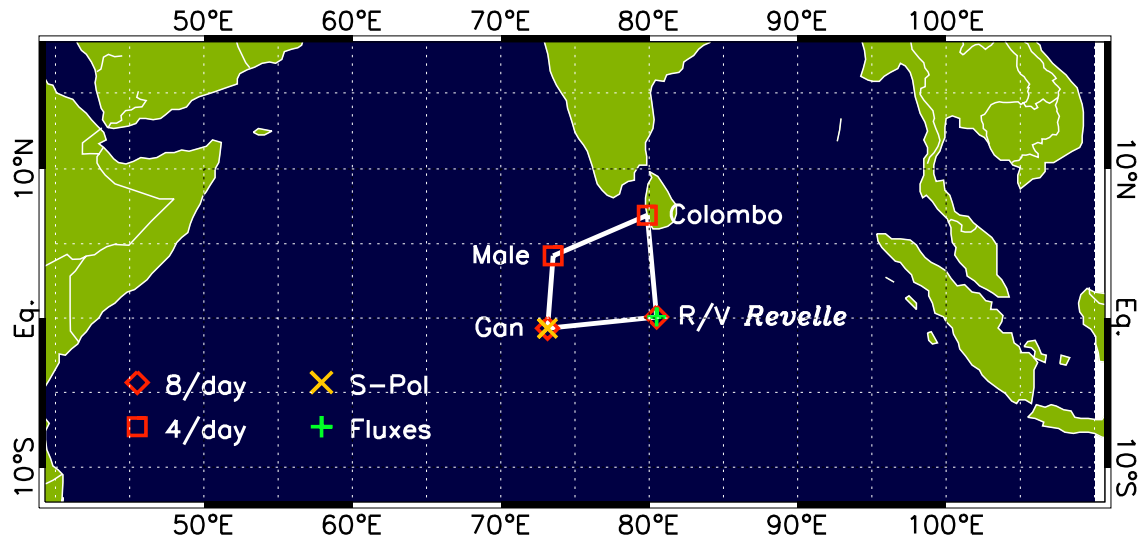
1040 FIG. 15. Diurnal composites of TRMM 3B42 rainfall (mm day^{-1}) averaged over the
 1041 northern sounding quadrilateral for the (a) Oct and (b) Nov suppressed phases.
 1042 Composite date ranges are (a) 7–13 Oct and (b) 11–16 Nov (end-dates are inclusive) (as
 1043 in Fig. 15, below). Local time is indicated along the abscissa.

1044 FIG. 16. Diurnal composite variables from the northern-array gridded analysis for the (a)
 1045 Oct and (b) Nov suppressed phases, with (from left–right) water vapor mixing ratio with
 1046 composite mean removed q' ($10^{-1} \text{ g kg}^{-1}$), ω (hPa day^{-1}), Q_1 , and Q_2 (K day^{-1}). Composite
 1047 date ranges are (a) 7–13 Oct and (b) 11–16 Nov (end-dates are inclusive). Horizontal
 1048 dashed lines indicate the 0°C level. Vertical smoothing has been applied to all fields
 1049 using a three-point running mean.

1050 FIG. 17. A model of MJO initiation based on DYNAMO observations. (a) Time–pressure
 1051 series of relative humidity (RH; ranging from 40~80%) and clouds, spanning the
 1052 suppressed phase, onset, and early-active phase (abscissa is time in days), *depicting only*
 1053 *variability on the MJO timescale*. Shown is an evolution from shallow cumulus to
 1054 congestus to deep cumulonimbus and stratiform clouds, with high cirrus clouds appearing
 1055 before onset. Open (closed) arrows indicate vertical (horizontal) motion, with size

1056 proportional to magnitude. (b) (top) Time–pressure series during the late-suppressed
1057 phase [denoted by the dashed box in (a)] of RH, clouds, and rainfall; and (bottom) the
1058 corresponding time series of anomaly SST (black-solid), daily-mean SST (dashed), and
1059 latent heat flux (red), *including diurnal variability* (abscissa ticks are local midnight). (c)
1060 Characteristic cloud field, as depicted by MODIS true-color imagery, in the (left)
1061 morning and (right) afternoon (from Figs. 11e,f), showing the prominence of mesoscale
1062 organization (i.e., open cells and horizontal convective rolls).

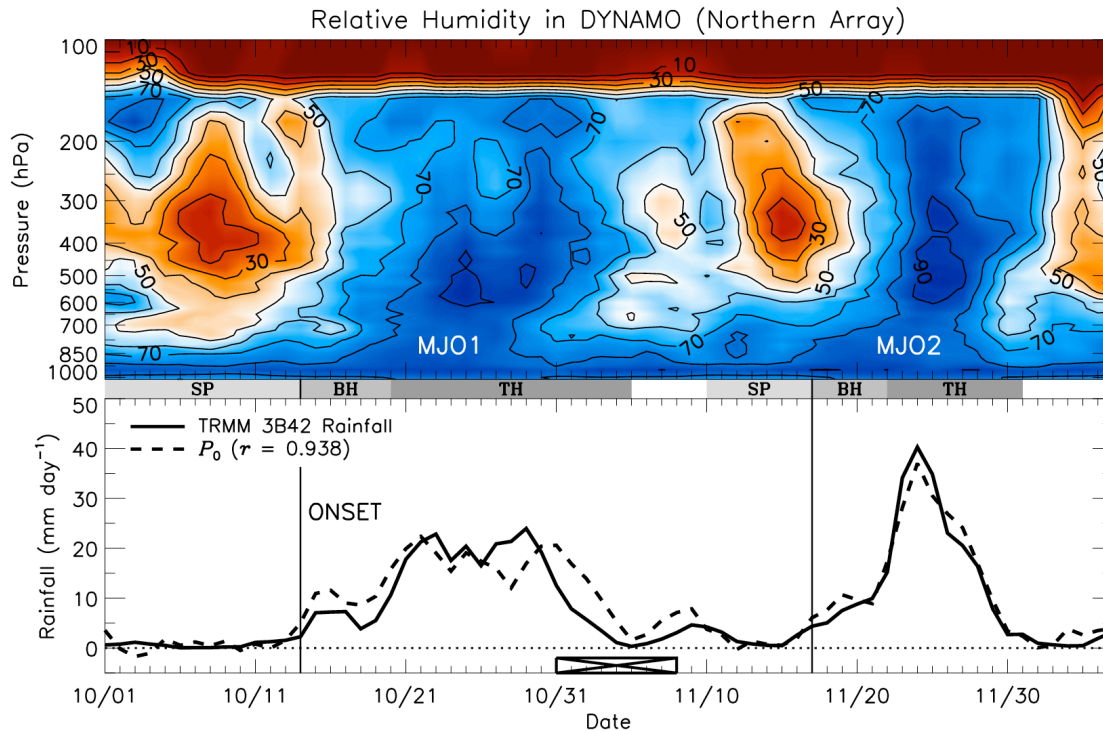
1063



1064

1065 FIG. 1. DYNAMO northern sounding array for the period October–December 2011.
 1066 Soundings were launched four–eight times per day, as indicated. Locations of the NCAR
 1067 S-Pol radar (Addu Atoll) and air-sea flux site (R/V *Revelle*) are also indicated.

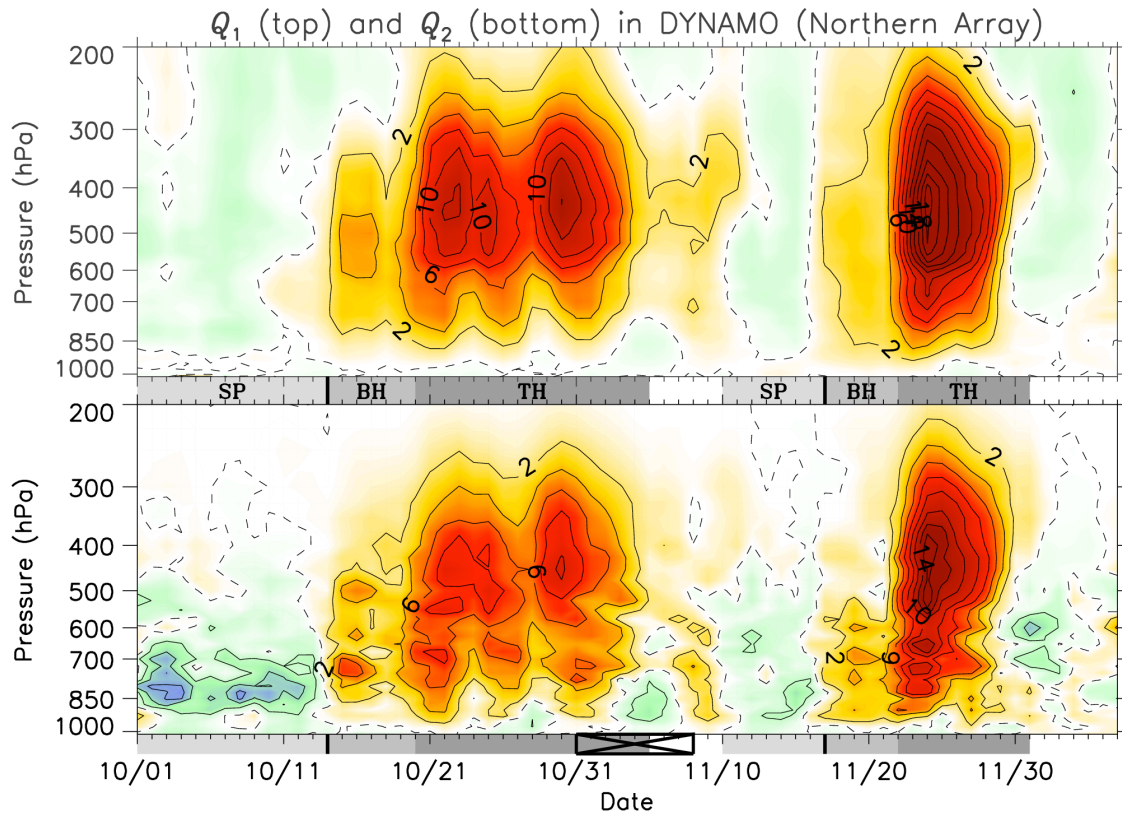
1068



1069

1070 FIG. 2. (top) Time–pressure series of daily-mean relative humidity RH (%; with respect to
 1071 ice where temperature $< 0^{\circ}\text{C}$) from the northern-array gridded analysis spanning the Oct
 1072 and Nov MJO events (MJO1 and MJO2, respectively). (bottom) Daily-mean rainfall
 1073 estimates (mm day^{-1}) from TRMM 3B42 (solid) and the moisture budget (4) P_0 (dashed).
 1074 Both fields have been temporally smoothed using a three-day running mean. Correlation
 1075 r between the smoothed rainfall estimates is indicated (significant to the 99% level using
 1076 the Student’s t-test and assuming a sample size of seven, the approximate number of ten-
 1077 day periods in the dataset). Here and in subsequent figures: “SP” refers to suppressed
 1078 periods, and “BH” (“TH”) to periods of bottom-heavy (top-heavy) apparent heating,
 1079 drying, and vertical motion profiles (Figs. 3 and 4) (see text for date ranges); the black
 1080 “X” along the abscissa indicates periods when the *Revelle* made a port call; and the
 1081 vertical lines denote MJO onset (i.e., when the apparent cooling and moistening switch to
 1082 heating and drying).

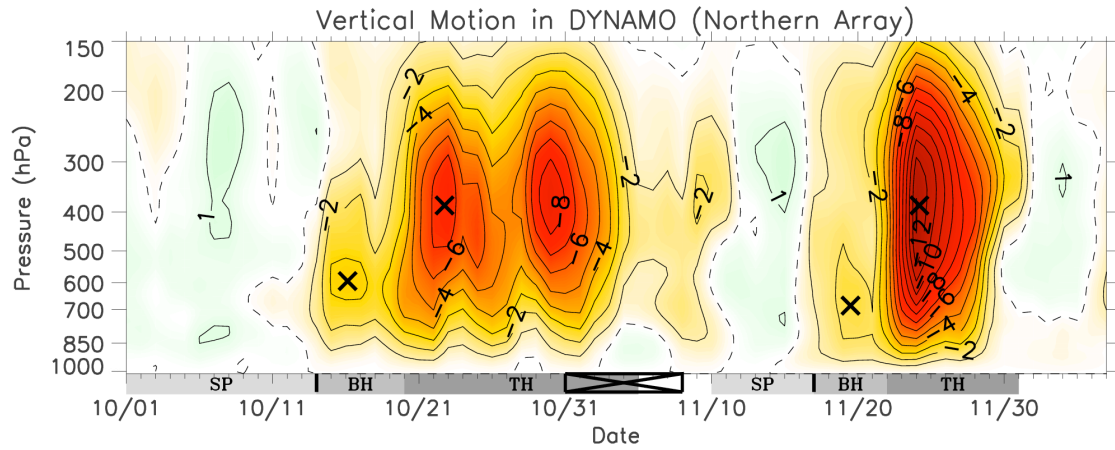
1083



1084

1085 FIG. 3. Daily-mean time–pressure series of the apparent heat source Q_1 (top) and apparent
 1086 moisture sink Q_2 (bottom) (K day^{-1}). The zero contour is dashed. Three-day temporal
 1087 smoothing has been applied.

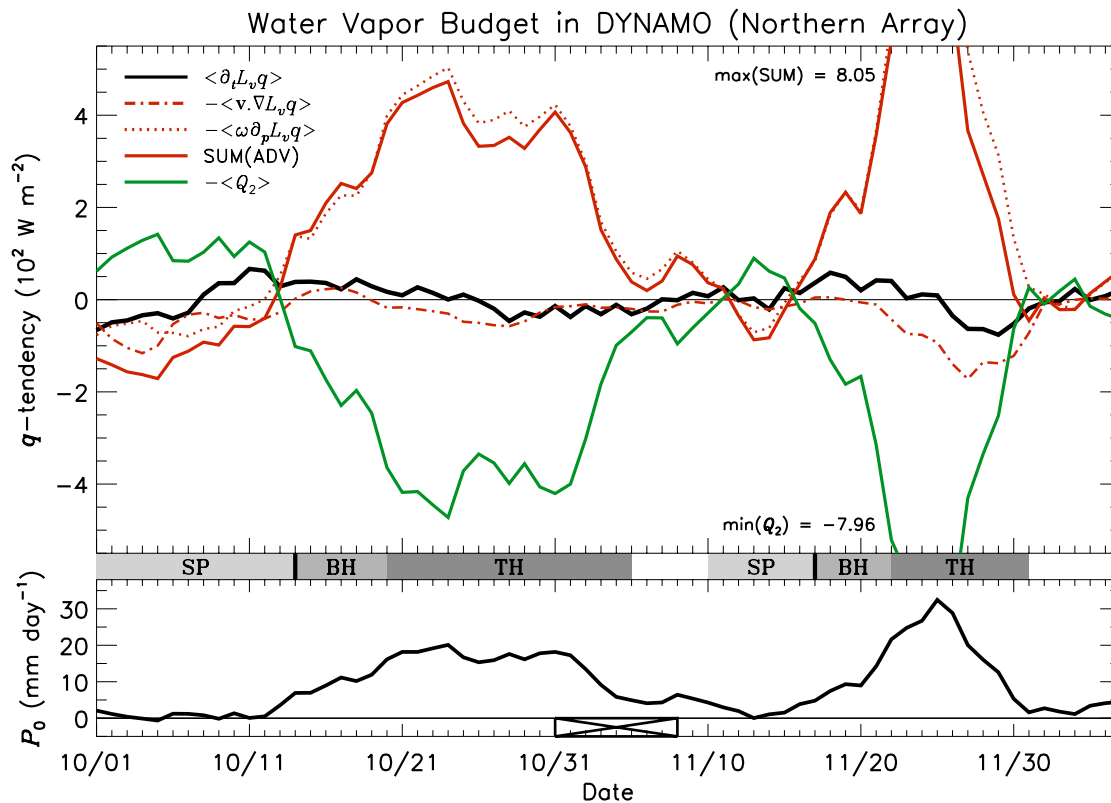
1088



1089

1090 FIG. 4. As in Fig. 3 except for vertical pressure velocity ω (hPa day^{-1}). X's are placed in
 1091 several places to highlight the shift of the level of maximum ascent.

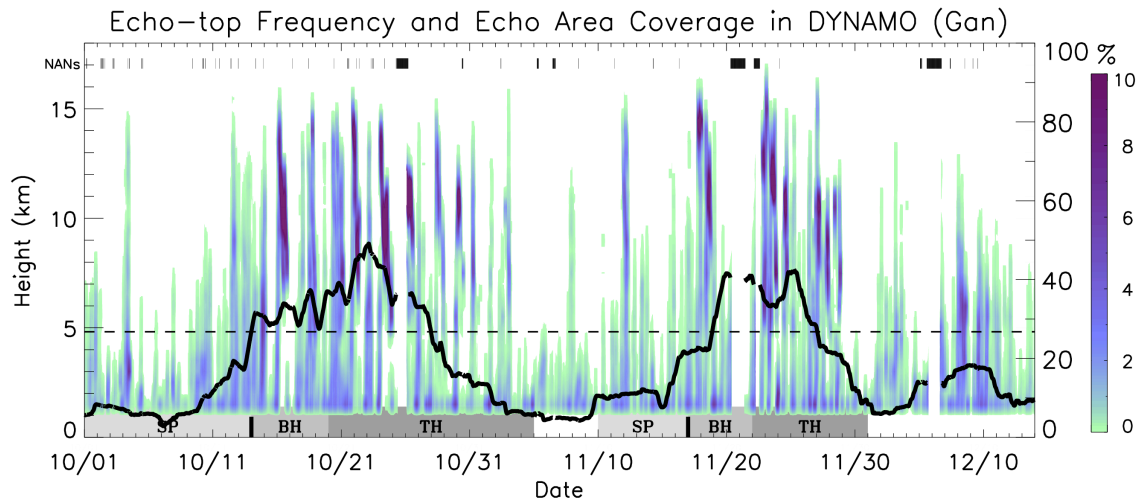
1092



1093

1094 FIG. 5. (top) Daily-mean vertically integrated water vapor budget (10^2 W m^{-2}) and
 1095 (bottom) P_0 (mm day^{-1}). Budget terms are calculated as shown in (5), with the local
 1096 tendency (black), horizontal advection (red, dot-dashed), vertical advection (red, dotted),
 1097 the sum of horizontal and vertical advection (SUM(ADV); red, solid), and apparent
 1098 sources (green). Maximum and minimum values for terms exceeding the ordinate scale
 1099 are indicated (top). Five-day temporal smoothing has been applied to all fields.

1100



1101

1102 FIG. 6. Time-height series of echo-top frequency and echo area coverage (%) from 15-

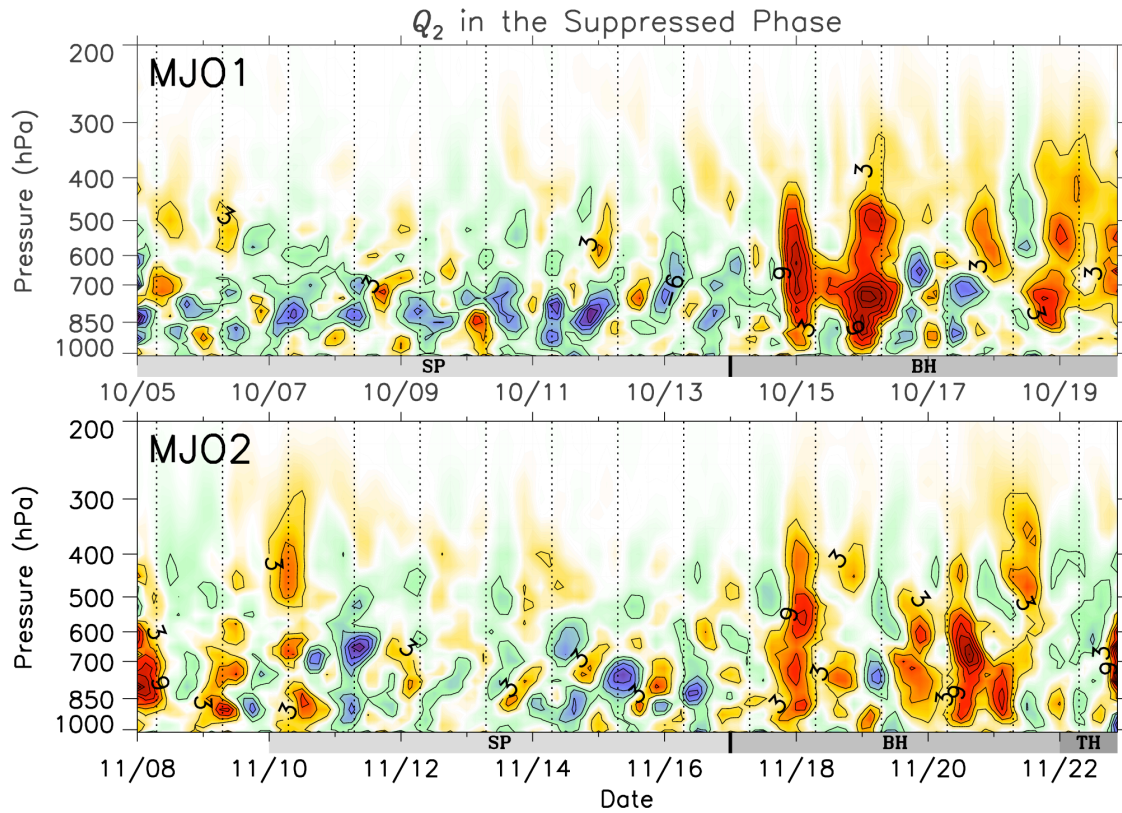
1103 min S-Pol RHI data. Temporal smoothing has been applied to echo-top frequency (echo

1104 area coverage) using a six-hour (five-day) running mean. Black hashes near the top

1105 indicate time periods of missing data (where the time gap between scans exceeded 23

1106 min). The dashed line indicates the 0°C level.

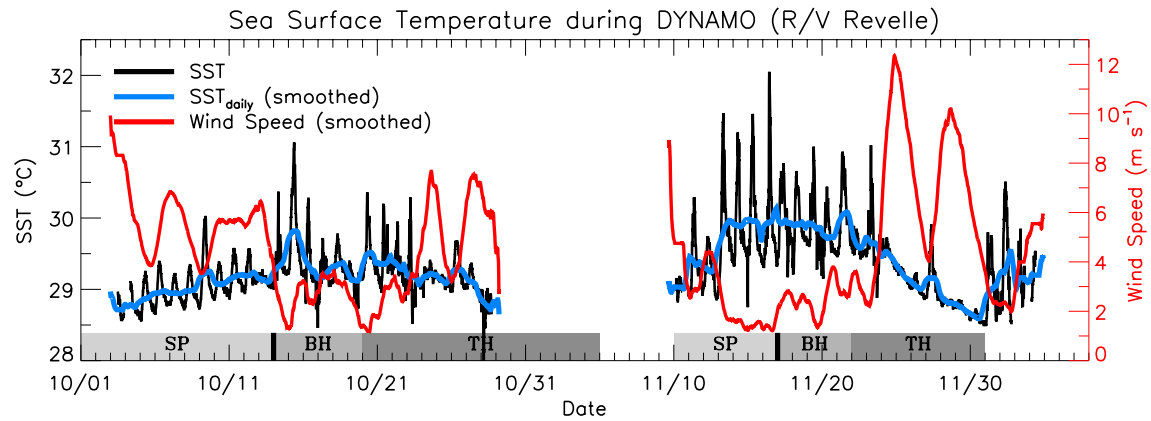
1107



1108

1109 FIG. 7. Time–pressure series of Q_2 (K day⁻¹) for the suppressed and early-active phases of
 1110 (top) MJO1 and (bottom) MJO2. The dotted vertical lines mark local noon. Three-point
 1111 smoothing has been applied in the vertical (i.e., over 50 hPa) and in time (i.e., over six
 1112 hours).

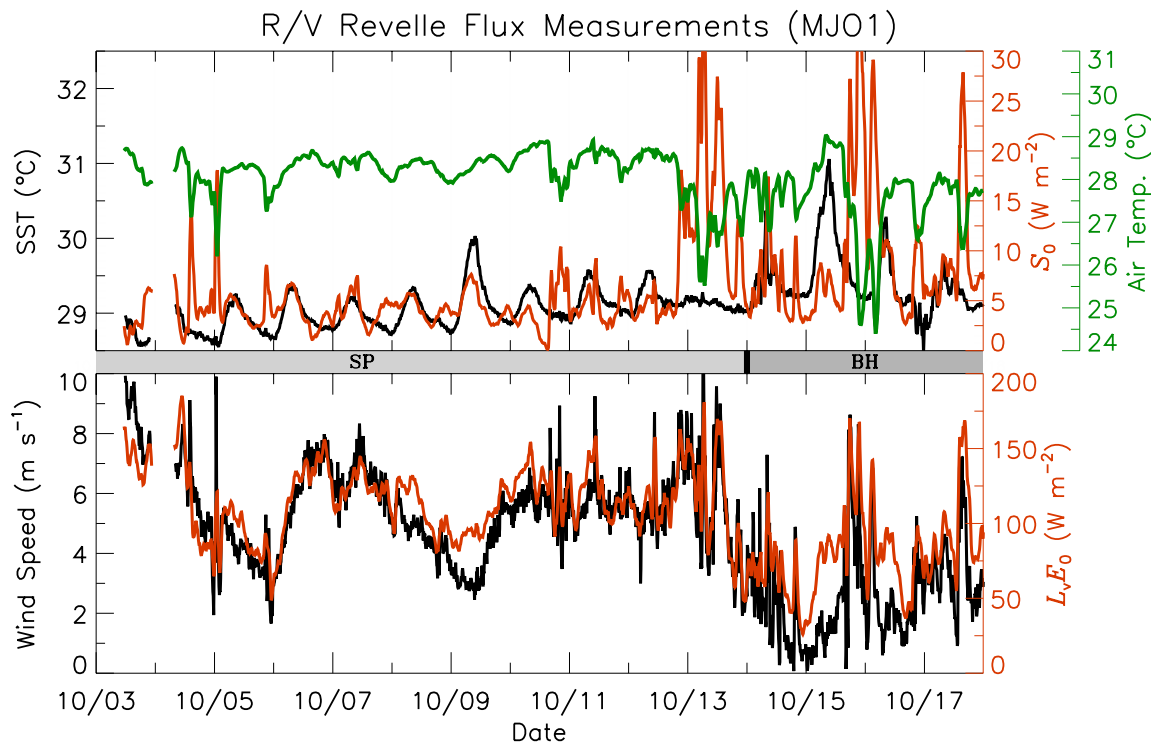
1113



1114

1115 FIG. 8. Time series of sea surface temperature (SST, adjusted to skin temperature; black;
 1116 °C; left axis), SST smoothed using a 24-h running mean (SST_{daily} ; blue), and surface
 1117 wind speed smoothed using a 24-h running mean (red; m s^{-1} ; right axis) from the *Revelle*
 1118 flux site. All fields from the *Revelle* flux site originate from 10-min data.

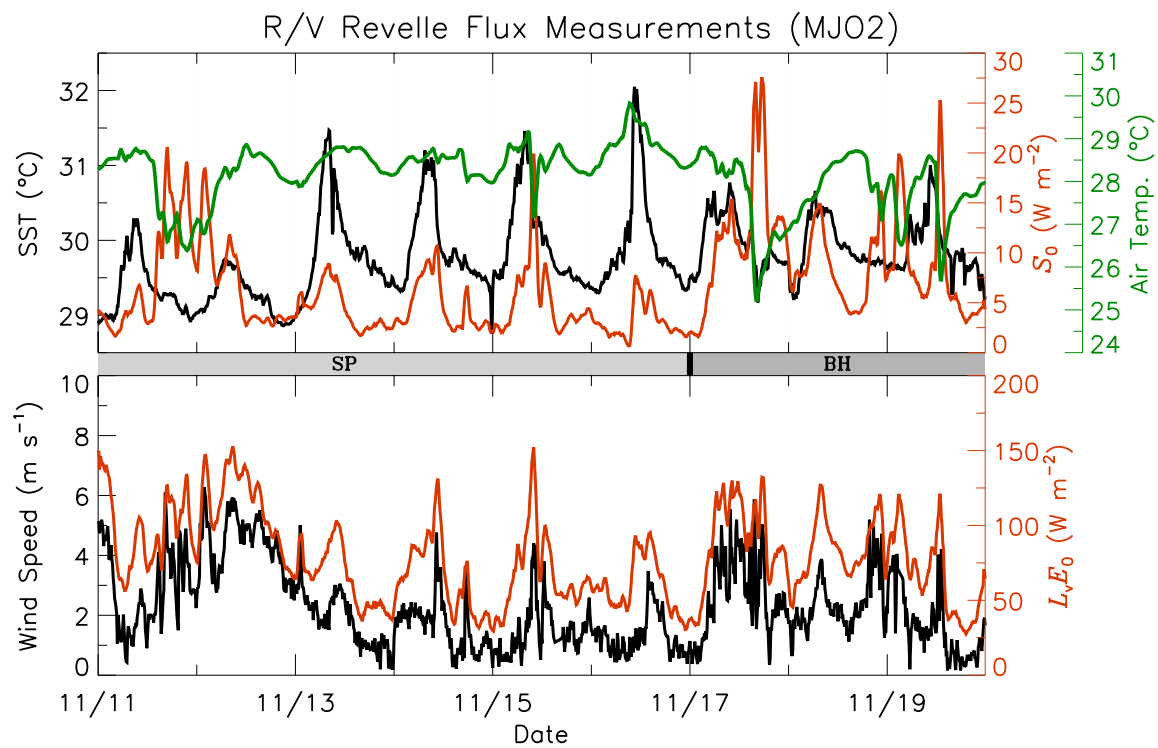
1119



1120

1121 FIG. 9. (top) Time series spanning the suppressed phase of MJO1 with SST (black; °C;
 1122 left axis), 10-m air temperature (green; °C; outer-right axis), and surface sensible heat
 1123 flux S_0 (red; W m^{-2} ; inner-right axis) from the *Revelle* (red; W m^{-2} ; right axis). (bottom)
 1124 As in the top except with wind speed (black; m s^{-1} ; left axis) and surface latent heat flux
 1125 $L_v E_0$ (red; W m^{-2} ; right axis). S_0 and $L_v E_0$ have been smoothed using a one-hour running
 1126 mean.

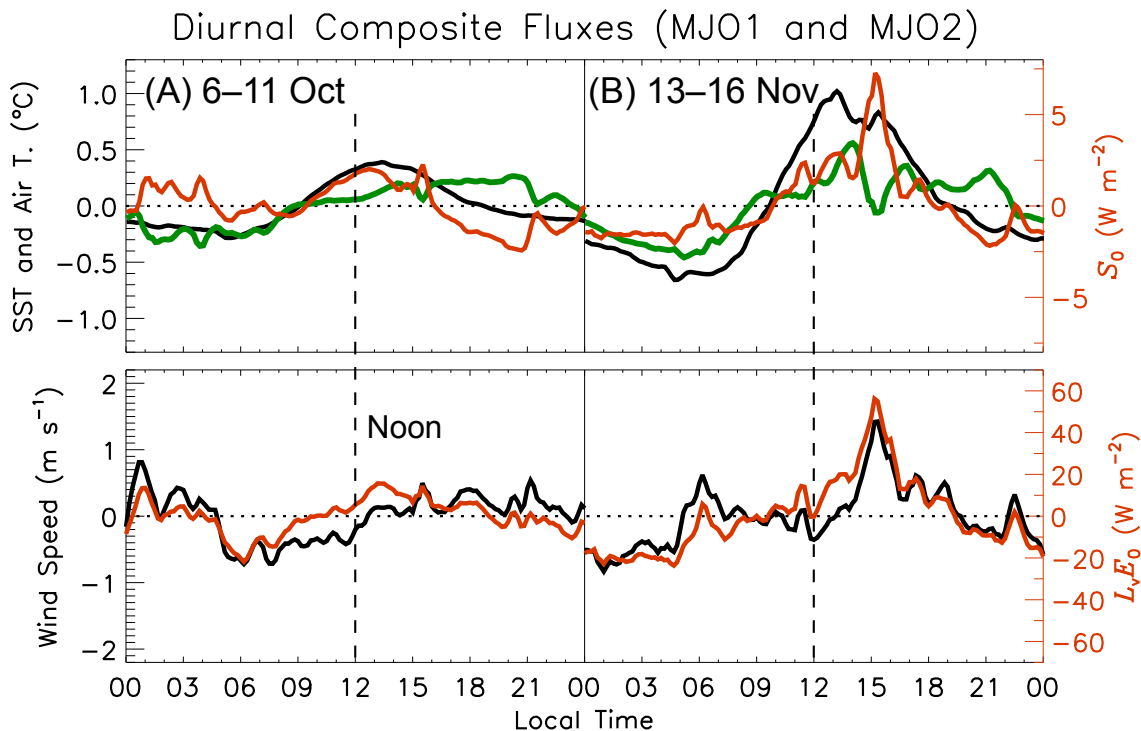
1127



1128

1129 FIG. 10. As in Fig. 9 except for the suppressed phase of MJO2.

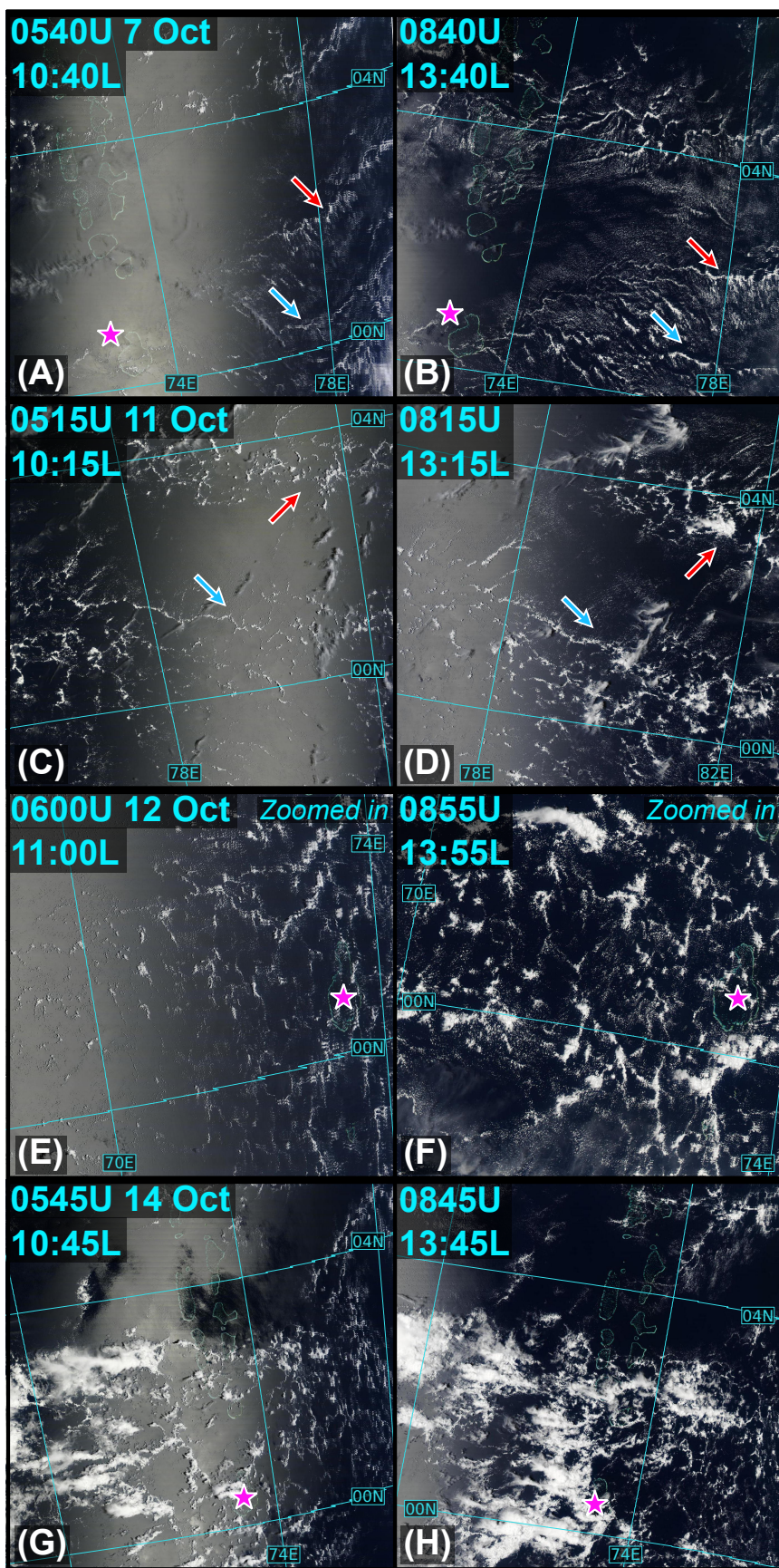
1130



1131

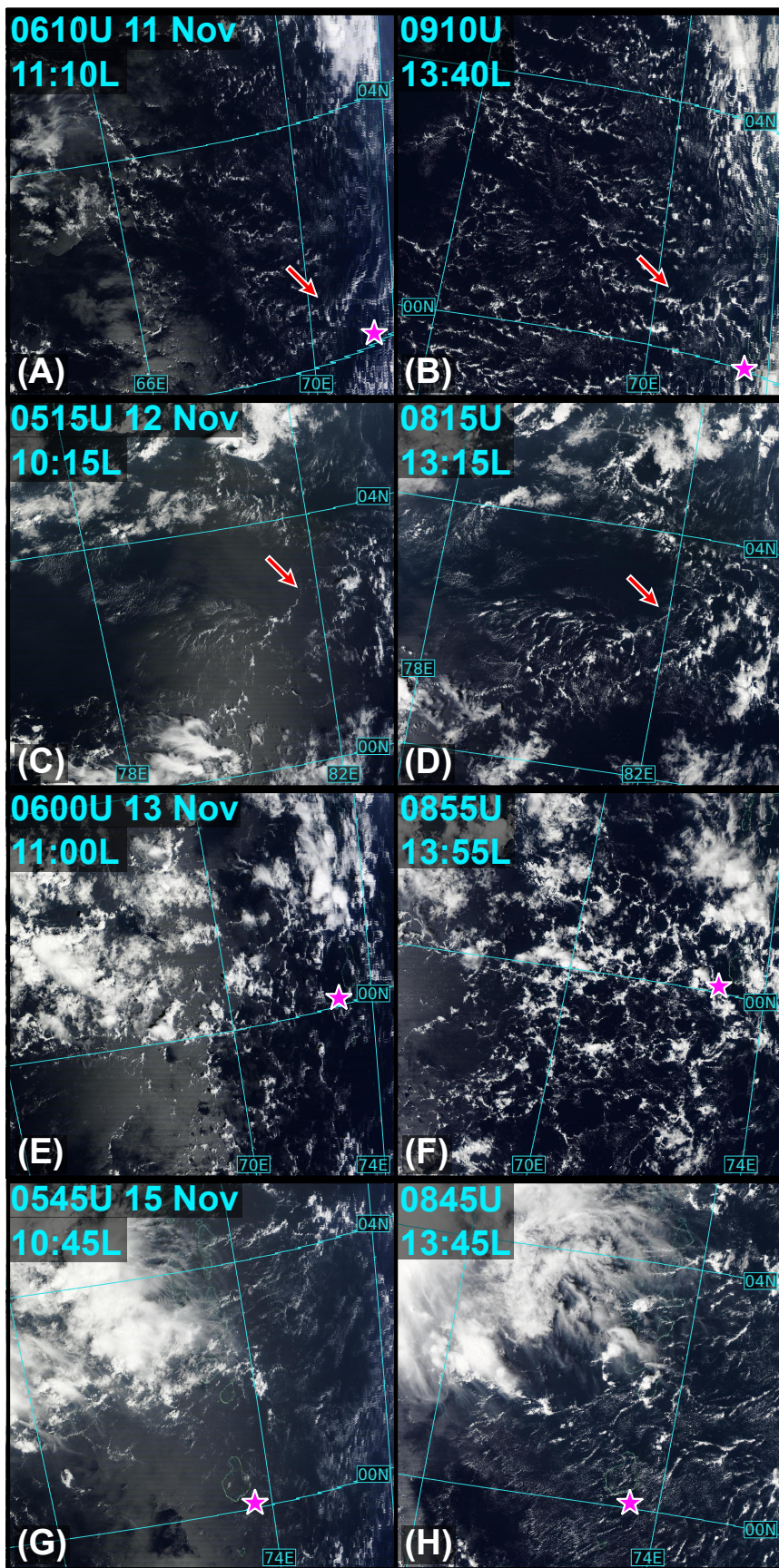
1132 FIG. 11. (top) Diurnal composite SST (black; °C; left axis), 10-m air temperature (green;
 1133 °C; left axis), and S_0 (red; W m^{-2} ; right axis) for the (a) Oct (MJO1) and (b) Nov (MJO2)
 1134 suppressed phases. Composite means have been removed. (bottom) As in the top except
 1135 with wind speed (black; m s^{-1} ; left axis) and surface latent heat flux $L_v E_0$ (red; W m^{-2} ;
 1136 right axis). Composite date ranges are (a) 6–11 Oct and (b) 13–16 Nov (end-dates are
 1137 inclusive). Local time is indicated along the abscissa. Vertical dashed lines indicate
 1138 local noon. All fields have been smoothed using a 30-min running mean.

1139



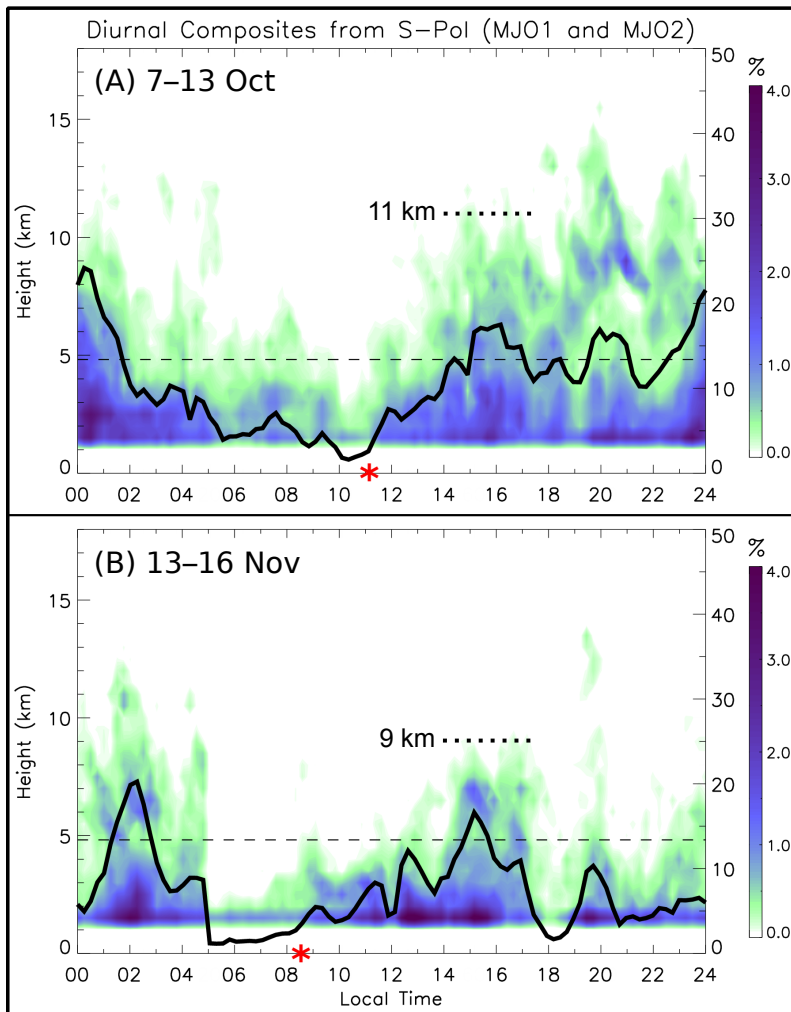
1141 FIG. 12. Cropped true-color images from the Terra (left) and Aqua (right) MODIS
1142 satellites for selected dates of the Oct suppressed phase (MJO1). Date is indicated in the
1143 left column, and UTC and local time are indicated in each panel. The magenta star marks
1144 Huvadhu Atoll, located ~100 km north of Addu Atoll. Red and blue arrows indicate
1145 subjectively identified corresponding cloud features between same-day images.

1146



1148 FIG. 13. As in Fig. 11 except for the Nov suppressed phase (MJO2).

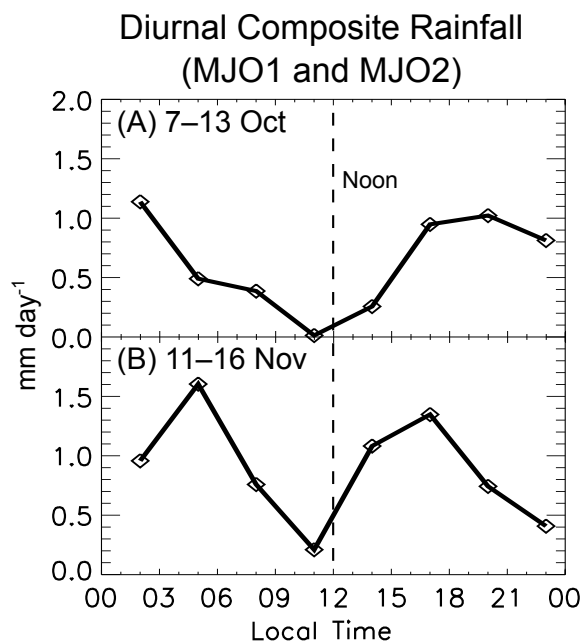
1149



1150

1151 FIG. 14. Diurnal time–height composites of convective echo-top frequency and echo area
 1152 coverage (%) for the (a) Oct and (b) Nov suppressed phases, calculated from 15-min S-
 1153 Pol RHI data. Composite date ranges are (a) 7–13 Oct and (b) 13–16 Nov (end-dates are
 1154 inclusive). Local time is indicated along the abscissa. Asterisks mark the time of
 1155 increasing echo-top frequency and echo area coverage. The 11- and 9-km levels are
 1156 indicated by dotted lines. Horizontal dashed lines indicate the 0°C level.

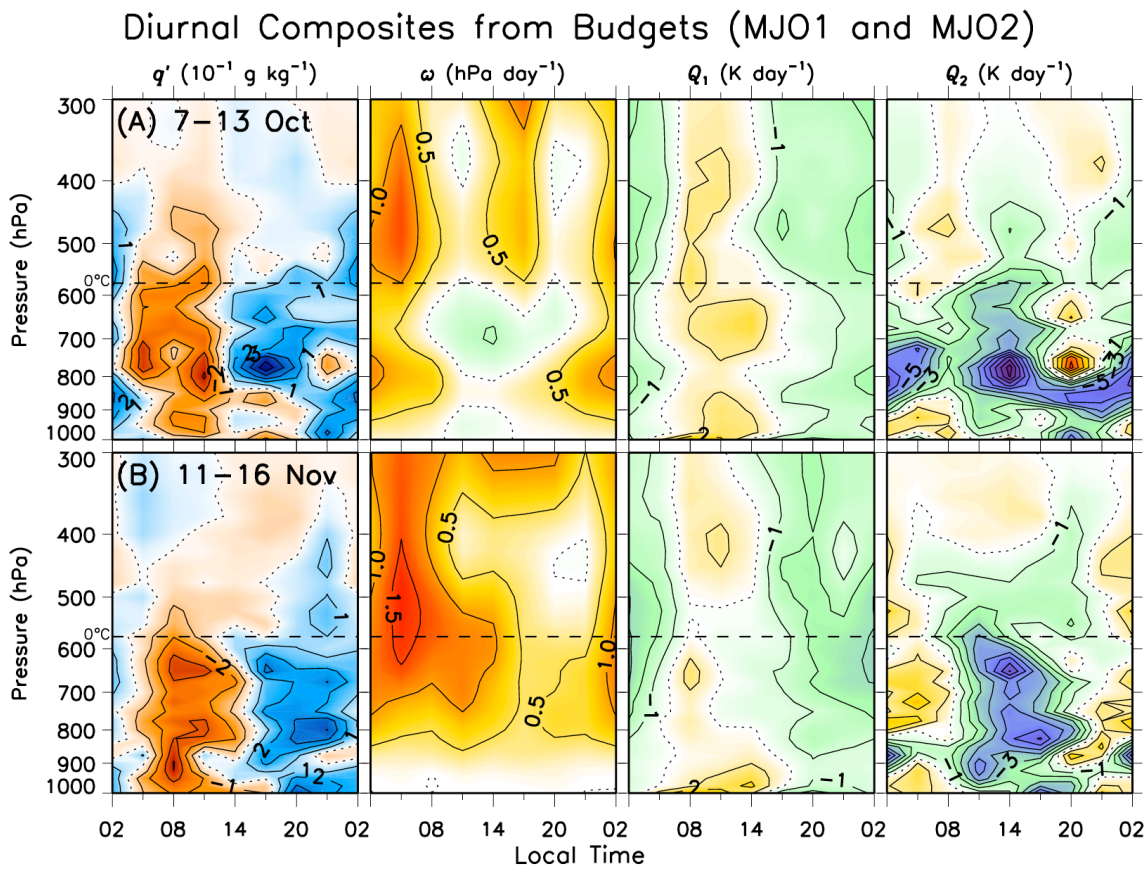
1157



1158

1159 FIG. 15. Diurnal composites of TRMM 3B42 rainfall (mm day⁻¹) averaged over the
 1160 northern sounding quadrilateral for the (a) Oct and (b) Nov suppressed phases.
 1161 Composite date ranges are (a) 7–13 Oct and (b) 11–16 Nov (end-dates are inclusive) (as
 1162 in Fig. 15, below). Local time is indicated along the abscissa.

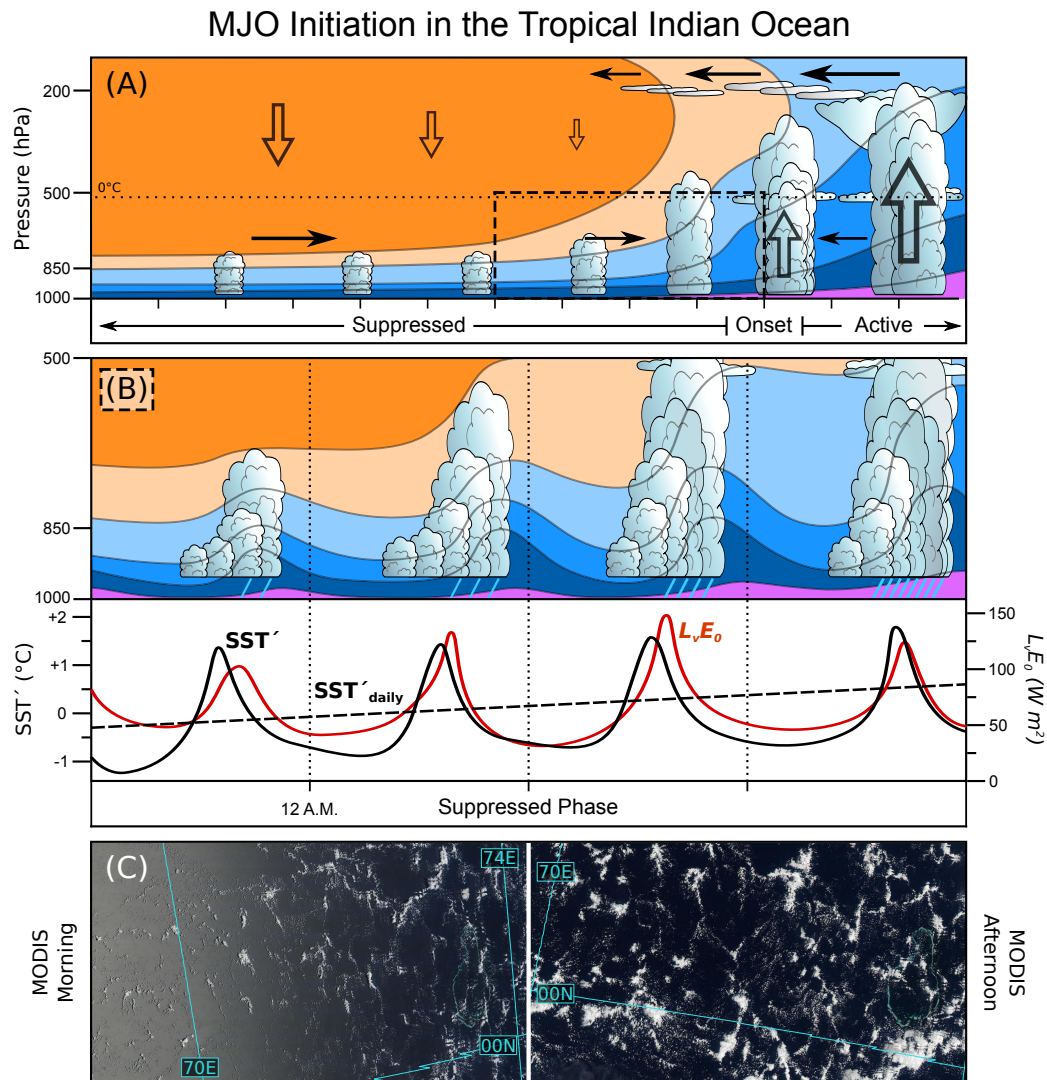
1163



1164

1165 FIG. 16. Diurnal composite variables from the northern-array gridded analysis for the (a)
 1166 Oct and (b) Nov suppressed phases, with (from left–right) water vapor mixing ratio with
 1167 composite mean removed q' ($10^{-1} \text{ g kg}^{-1}$), ω (hPa day^{-1}), Q_1 , and Q_2 (K day^{-1}). Composite
 1168 date ranges are (a) 7–13 Oct and (b) 11–16 Nov (end-dates are inclusive). Horizontal
 1169 dashed lines indicate the 0°C level. Vertical smoothing has been applied to all fields
 1170 using a three-point running mean.

1171



1172

1173 FIG. 17. A model of MJO initiation based on DYNAMO observations. (a) Time–pressure
 1174 series of relative humidity (RH; ranging from 40~80%) and clouds, spanning the
 1175 suppressed phase, onset, and early-active phase (abscissa is time in days), *depicting only*
 1176 *variability on the MJO timescale*. Shown is an evolution from shallow cumulus to
 1177 congestus to deep cumulonimbus and stratiform clouds, with high cirrus clouds appearing
 1178 before onset. Open (closed) arrows indicate vertical (horizontal) motion, with size
 1179 proportional to magnitude. (b) (top) Time–pressure series during the late-suppressed
 1180 phase [denoted by the dashed box in (a)] of RH, clouds, and rainfall; and (bottom) the
 1181 corresponding time series of anomaly SST (black-solid), daily-mean SST (dashed), and
 1182 latent heat flux (red), *including diurnal variability* (abscissa ticks are local midnight). (c)

1183 Characteristic cloud field, as depicted by MODIS true-color imagery, in the (left)
1184 morning and (right) afternoon (from Figs. 11e,f), showing the prominence of mesoscale
1185 organization (i.e., open cells and horizontal convective rolls).